BOSEMAN, ADAM J., Ph.D. Study of Nanoscale Structural Biology Using Advanced Particle Beam Microscopy. (2015)
Directed by Dr. Dennis R. LaJeunesse. 89 pp.

This work investigates developmental and structural biology using current advancements in particle beam microscopy. Typically the examination of micro- and nanoscale features is performed using scanning electron microscopy (SEM), but in order to decrease surface charging, and increase resolution, an obscuring conductive layer is applied to the sample surface. As magnification increases, this layer begins to limit the ability to identify nanoscale surface structures. A new technology, Helium Ion Microscopy (HIM), is used to examine uncoated surface structures on the cuticle of wild type and mutant fruit flies. Corneal nanostructures observed with HIM are further investigated using a combination of focused ion beam milling and scanning electron microscopy (FIB/SEM) to provide detailed three dimensional information about internal events occurring during early structural development. These techniques are also used to reconstruct a developing mosquito germarium in order to characterize components involved in early oogenesis. Findings from these studies, and many more like them, will soon unravel many of the mysteries surrounding the world of developmental biology.

STUDY OF NANOSCALE STRUCTURAL BIOLOGY USING ADVANCED PARTICLE BEAM MICROSCOPY

by

Adam J. Boseman

A Dissertation Submitted to
the Faculty of the Graduate School at
The University of North Carolina at Greensboro
in Partial Fulfillment
of the Requirements for the Degree
Doctor of Philosophy

Greensboro
2015

Approved by

_____
Committee Chair

To my wife, Kristin. Thank you for your continued encouragement and support through all of these years

APPROVAL PAGE

This dissertation has been approved by the following committee of the Faculty of The Graduate School at The University of North Carolina at Greensboro.

Committee Chair _____
Dennis R. LaJeunesse

Committee Members _____
Daniel Joseph Christian Herr

_____
Joseph M. Starobin

_____
Ethan Will Taylor

_____
Date of Acceptance by Committee

_____
Date of Final Oral Examination

TABLE OF CONTENTS

Page

LIST OF FIGURES

Page

CHAPTER I

BACKGROUND

1.1 Historical Achievements in Microscopy

Microscopy has been used by humans for thousands of years now. As far as we know, the Egyptians were the first to make convex lenses around 2600 BC using crystals. Once the remarkable optical properties caused by light passing through a lens were realized, people were driven to further refine lenses and create many invaluable tools used today. Eye glasses, telescopes, and hand lenses (magnifying glasses) are just a few examples. During the late 16th century the first rudimentary microscopes were created with hand lenses affixed to a device with a base an area to fasten a specimen for viewing. The first compound microscope was made in 1590 by Zacharias Janssen, achieving a 10x magnification. Using a similar microscope Robert Hooke published his observations on cork and lice in in his 1665 article "Micrographia" [HG61]. Hooke's findings led to an increase in personal hygiene in seventeenth century England [CR09].

The resolution of the microscopes increased along with the increase in the quality of lenses being made. Around the turn of the 17th century Antoine Van Leuwenhoek (using his closely guarded advanced knowledge of lens making) was able to create a single lens microscope with the ability to magnify over 250 times, giving it a resolution of about 1μm. His findings of the structure and life of bacteria, sperm, protozoa and many neural tissues were reported to the Royal Society in London between 1673-1690. Soon the microscope became more and more advanced with things like

rack-and-pinion stage movements by Bonanni in 1690, multi-lens eye pieces, and the lens turret by George Adams in the 1740s [CR09]. It wasn't until the 19th century though that the wavelike nature of light was discovered. This allowed the behavior of light to be studied in much more detail, and led to many advancements in lens and microscope quality. In 1873 it was recognized that the ultimate resolving power of a light microscope was not unlimited. After the introduction of modern physics in the early 20th century, the limiting resolution was realized [SS93].

With the increasing popularity of photography in the late 1800s also came the coupling of the microscope with the camera. This allowed images seen in the microscope to be captured on film, and displayed outside of the microscope for the first time. Cameras were soon replaced by video recorders and live videos of small objects could be taken. Further advances in computers in the 1980s has led to the replacement of film with digital imaging devices.

Other microscopic imaging techniques were also introduced in the twentieth century that have led to advances many areas of science. Heimstaedt and Lehmann developed fluorescence microscopy technology. This allows specific organelles of cells to be tagged and highlighted in the microscope for visualization. Phase contrast optics, developed by Zernike, used both diffracted and non diffracted light to image biological specimens without needing to stain them. Improving on the design of the Wollaston prism, George Nomarski was able to take clear images of optical sections, giving the first 3D reconstruction of a live cell [CR09]. In the late 1980s fluorescent microscopy and optical sectioning were combined to form laser scanning confocal microscopy, which can create a 3D reconstruction of a specimen with sub-micrometer resolution. More recently, techniques have been introduced that use clever methods to

break through the ultimate resolution limit of optical microscopy. Researchers have been able to resolve features on the order of tens of nanometers using these super resolution microscopy techniques [SVELS12].

1.2 Scanning Electron Microscopy

Many people's eyes constantly use light to form the world in which they interact, at least while they're awake. Using electrons to obtain information is less familiar to most of us because it doesn't rely on the visible spectrum of energy. This allows us to see things in a completely different way. One of the interesting results is in electron/ion microscopy, where one can image things much smaller than could be allowed with the most powerful optical microscopes. A scanning electron microscope (SEM) rasters a beam of electrons across an are of a specimen to recreate an image of the surface in digital form. The electron beam is scanned across a surface pixel by pixel (for whatever resolution the user sets). The signals emitted from each spot can then be gathered by a detector and analyzed to generate a great amount of data about the specimen.

Primary electrons from the electron beam are bombarded onto the surface of a specimen to generate different types of signals. Interactions from these primary electrons can occur from relatively deep inside the surface of the specimen depending on the accelerating voltages used. There are a number of different signals generated each time the electron beam interacts with a specimen's surface. These include secondary electrons, backscattered electrons, characteristic x-rays and more, they originate from different depths within the surface with secondary electrons being closest to the surface and characteristic x-rays coming from the deepest layers of the material.

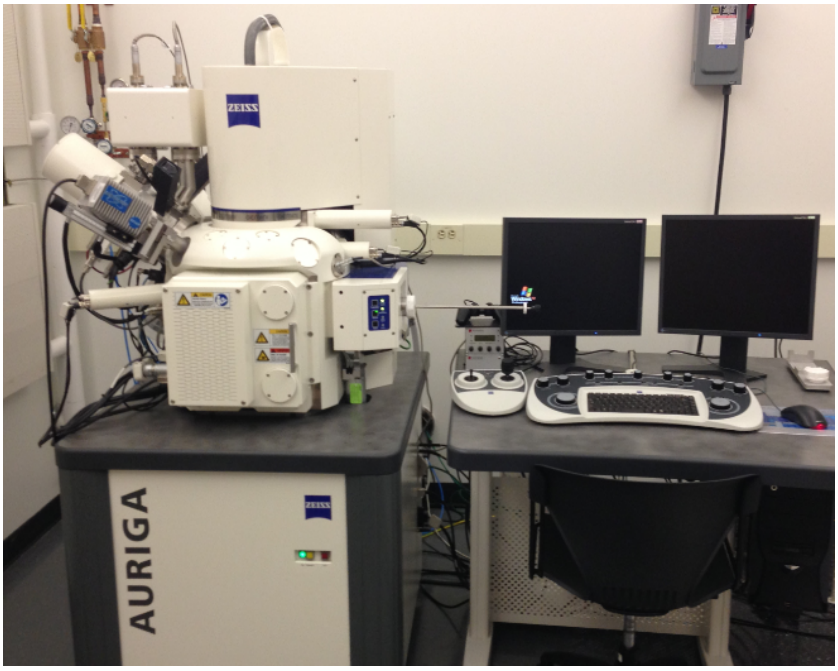

Figure 1. Zeiss Auriga FIB/SEM

Each of these signals are collected by a different detector and analyzed by computer software to give the user information about an area being analyzed. A Zeiss Auriga SEM fitted with many different types of detectors is shown in Figure 1.

A commonly used type of detector is the secondary electron (SE) detector. It is used to collect inelastically scattered, low energy (less than 50eV), electrons coming from inner shell orbitals. These electrons are ejected from a close proximity to the sample's surface (5-10nm) after being hit with the primary electron beam, and are collected and analyzed to give a greyscale image that is useful for topographical and spatial orientation of features on a specimen's surface [CR09]. The grey value for each pixel is determined by the number of secondary electrons emitted after a spot is irradiated with the electron beam. The image is formed by collecting secondary electrons as the beam is scanned pixel by pixel across the surface.

Figure 2. Secondary Electron Image of a Fruit Fly (*D. melanogaster*).

Those values are then plotted in two dimensions. The number of pixels is set by the user as the image resolution. An SEM image can give a great amount of detail since the secondary electrons are generated from so close to the surface, even at low magnifications. This can be seen in the SE image of a common fruit fly (*D. melanogaster*) shown in Figure 2. This SEM is also equipped with another secondary electron detector called an InLens detector.

Backscattered electrons are another type of signal generated from bombardment of the primary electron beam onto a surface. These elastically scattered, high energy (over 50eV), electrons are be produced from deeper within the surface being bombardes and arecollected by a backscattered electron detector (BSD). The detector is

located directly below the pole piece that the primary electron beam exits through. Information from the BSD is different than the type of information gleaned from the SE detector because the energy of a backscattered electron can be used to determine information about the element it came from. Backscattered electrons can also cause noise in an image because they can create secondary electrons far away fro where the beam initially hits.

After an inelastic scattering event produces a secondary electron, the atom has a electron hole left open. In order for the atom to stabilize an outer shell electron drops down to fill the hole. A characteristic x-ray is produced when the electron drops down from an outer to inner shell orbital. A unique energy spectrum for each element can be produced by irradiating a spot with the electron beam and detecting the resulting x-ray energies. Each shell of every atom has its own characteristic energy, thus elemental detection and analysis can be performed.

1.3 Focused Ion Beam Microscopy

Aside from the source, a focused ion beam (FIB) microscope is very similar to an SEM. Instead of relying on electrons, a FIB system uses heavier element ions, typically gallium, to produce the primary beam. The difference is that bigger gallium ions are able to obtain high enough energies to mill away features, precisely and accurately, on a surface at the nanoscale. This can be useful in many areas of science from materials fabrication and characterization to developmental biology.

When a FIB system is combined with an SEM (FIB/SEM) it is possible to image with an electron beam while a sample is being milled with an ion beam, giving a real-time view of a sample as it is being processed/fabricated. To get accurate an milling

the microscope stage, or feature being milled, must be tilted so that it is normal to the FIB. This makes the SEM image somewhat skewed and requires an image correction process to correct. When done properly this enables the user to instantly see what is being milled. This also allows for serial imaging, or 3D milling, to take place. A 3D volume of a sample can be reconstructed by taking serial images of a freshly exposed block-face as it is being milled after each slice, and then reconstructing the images in a series. In order to get quality 3D data the pixel size of the images taken to be matched, or scaled, to the thickness of the slices taken by the FIB. As long as the slices the FIB takes are smaller than the features of interest, it is possible to get a cross-sectional view from any plane in the milled volume.

There are a number of other features used in combination with the FIB system depending on the desired application. One typically used system is a gas injection system (GIS). This system disperses a stream of a precursor gas into the ion beam. Interaction with the FIB causes the gas to deposit on areas specified by a predetermined process. Platinum and carbon are typically deposited as protective layers to cover a feature before milling, but there are an endless number of applications this process could be used for.

Another commonly used instrument along with the FIB is the nanomanipulator. This is usually a thin pointed shaft that has one or more degrees of movement, but can be a very carefully fabricated instrument. The nanomanipulator can be used to move objects very precisely inside the chamber of the microscope. The combination of FIB with GIS and the nanomanipulator can be used as a much more reliable technique to obtain TEM samples.

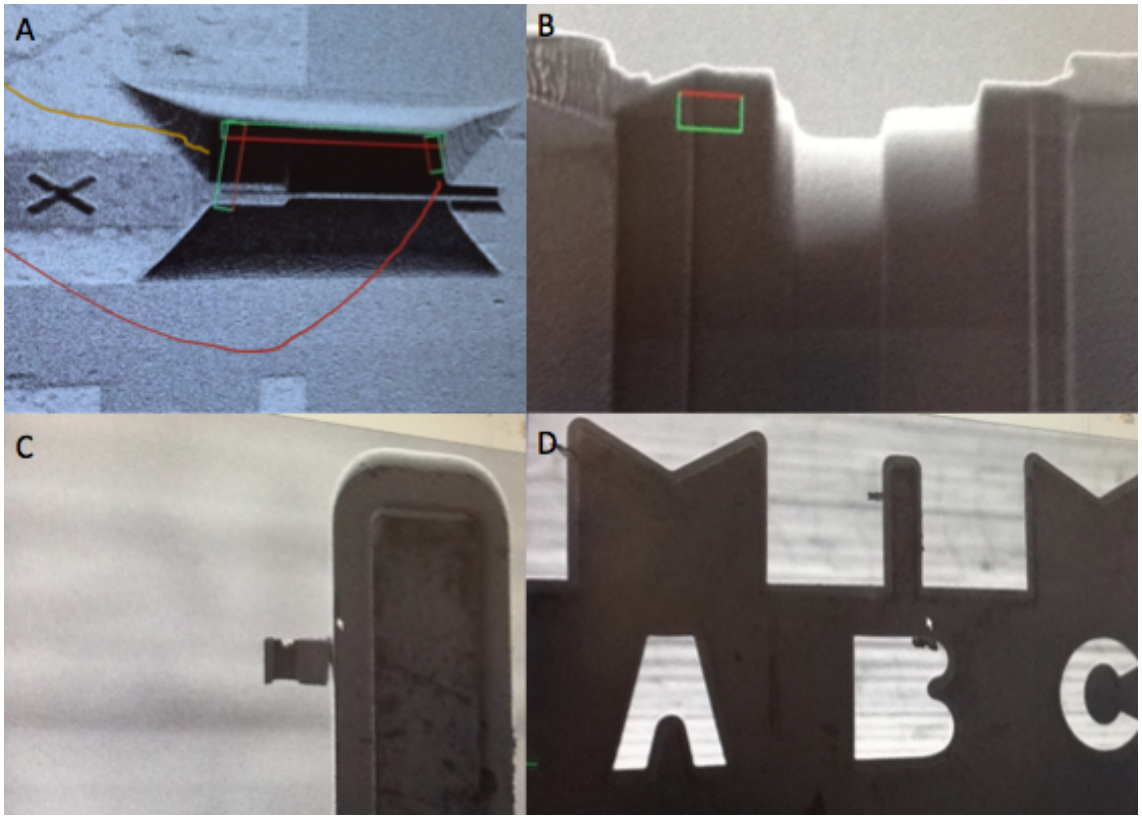

Figure 3. Process of Using the FIB to Cut TEM Lamella. A) Area selected and milled to leave a thin portion remaining. B) Lamella is tinned until it becomes electron transparent using FIB. C) Lamella is placed on TEM grid. D) View of TEM grid.

The FIB can be used to cut and thin a small section of material while the GIS system and manipulator can move and place the sample onto a specific location on a TEM grid. This process can be seen in Figure 3. Figure 3.A shows where an alignment mark was milled to allow for the stage to be rotated while milling out material from around the thin section to be used as the TEM lamella. The top line indices the pattern to be milled that will cut the lamella away from the surface, while the bottom line indicates a small gap left to hold the lamella. This small area is used to connect the

nanomanipulator tip before lifting the lamella from the surface. Figure 3.B shows how the lamella is thinned by the FIB until it becomes electron transparent. The area in the middle of the image becomes brighter indicating electron transparency. Figure 3.C and D show the lamella attached to the TEM grid.

1.4 Helium Ion Microscopy

In the fields of fabrication and lithography, HIM offers many advantages over traditional particle beam methods like focused ion beam (FIB) milling with gallium ions and scanning electron microscopy (SEM). HIM combines the advantages gained from a small beam size and high brightness, along with the increased particle momentum and SE yield, to fabricate features with a high level of control. Ion milling is a standard fabrication method that involves the removal of the substrate with a focused ion beam. Samples milled with standard FIB using gallium ion (Ga^+) sources often have residual contamination introduced by Ga^+ implantation during the milling process which can lead to alteration of the surface chemistry. Moreover, the more massive Ga^+ ions are harder to manipulate and control than He ion by possess a greater momentum when compared to helium ions which often results in unwanted sample damage especially when milling at the sub-30 nm scale [RS97], [FCFZ12]. This side-effect is not present in the HIM where sub-10nm features can be milled with high fidelity. Recently, intricate and detailed devices have been milled with HIM lithography that match the theoretical resonance quality factor limit modeled in a coaxial plasmonic nanoresonator [MPG$^+$13]. These structures would have been impossible with Ga^+ FIB milling. Rudneva et al. have developed a heating stage allowing milling of nanoscale patterns in Si and Ti. This has been able to demonstratt that, unlike

other methods, HIM milling did not affect the crystalline structure of the samples [RvVM$^+$13].

The HIM can be used in a variety of biological applications as well. Not only is it capable of imaging uncoated biological samples at a very high resolution [BNA$^+$13], [VBFSHW12], [BARB12], but it has also been used to mill nanopores with diameters below 4nm that are comparable to similar pores formed using TEM [YFS$^+$11]. Further studies have used related the milling depth to the ion dose for both direct and transmission milling shedding light into differences in milling parameters [MYH12]. The milling process allows for multiple diameter sizes on one sample and only takes seconds to mill one pattern, making it an ideal method for wafer-scale production.

All of the advantages arising from the gas field ion source (GFIS) with the helium beam have also made HIM a promising technique for ion lithography, or the patterning of a resist material by exposure to the ion beam. Until recently, these types of patterns have been written using electron beam lithography (EBL), or Ga^+ FIB, however these techniques are limited in the resolution of features by the spot size and the interaction volume of the beam itself. Micrometer range scattering due to the small particle size of the electron beam gives a large interaction volume at the surface while the gallium beam is good up to a certain point, but loses resolution below 30nm because of its relatively large beam size [MPG$^+$13].

Initially helium ion lithography (HIL) in hydrogen silsesquioxane was shown to be capable of achieving 20nm pitch dense structures with little resist residue, but had considerable resist residue with 10nm pitch structures [WCM$^+$09]. Although there were difficulties in obtaining sub-10nm structures, the required ion dosage was shown to be approximately an order of magnitude less than that needed with EBL.

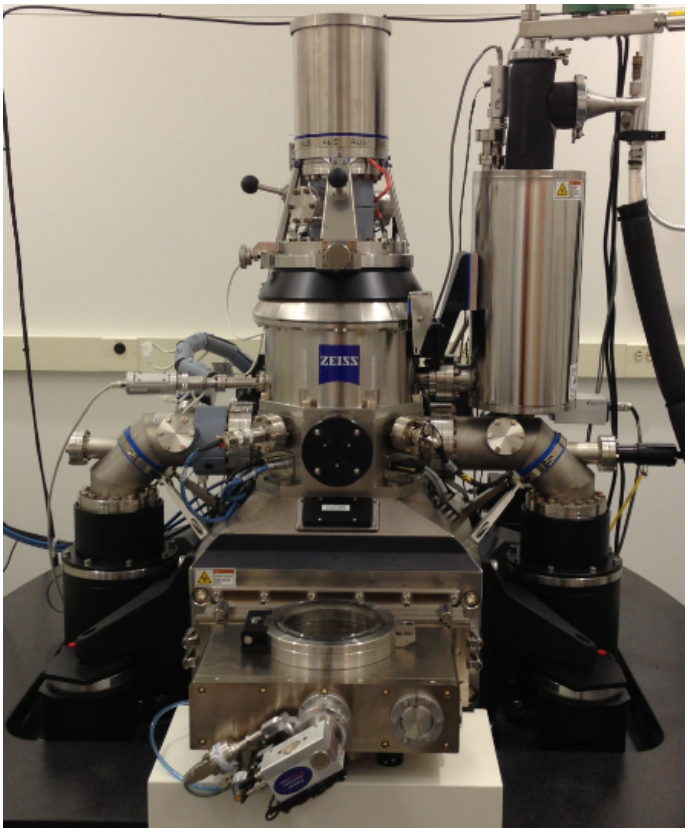

Figure 4. Zeiss Orion Plus HIM

The point spread function was also measured and had a reduction in the amount of micrometer range scattering similar to what is observed with electrons. Given these advantages, in its current state HIL has feature resolution comparable to EBL and recently, 4nm half pitch dense patterns have subsequently been achieved using HIL [LWSW12]. These structures were subsequently used for imprint lithography on a UV curable resist, demonstrating that high-throughput single-digit nanometer fabrication of dense patterns is possible using HIL.

HIL will continue to develop and will be a major player in single-digit nanometer fabrication and lithography. The development of other ion beam milling stations

using other noble gases such as neon, is now being explored as a lithography tool. The neon beam allows for an increased sensitivity to resist exposure. Neon ions have been shown to be ∼10X more sensitive than He and ∼1000X more sensitive than electrons and has resolution equal to state of the art EBL [WMN+11]. It can be sure that this technology will be refined as it continues to mature, and will surely have a great effect on many research areas relying on scanning particle beam lithography. While, much of HIM lithography has been concentrated on milling and processing non-polymeric materials such as SiO_2, as with other lithography methods it is simply a matter of time until the precision of HIM lithography will be applied to polymers.

CHAPTER II

HIM ANALYSIS OF *D. MELANOGASTER*

Insects have evolved numerous adaptations to survive a variety of environmental conditions. Given that the primary interface between insects and the environment is mediated through their skin or cuticle, many of these adaptations are found in extraordinary cuticle diversity both in morphology and structure. Not all of these adaptions manifest themselves in changes in the chemical composition of the cuticle but rather as elaborations of the surface structures of the cuticle. High resolution characterization of nanostructures on the cuticle of *Drosophila melanogaster* and other biological specimens has been carried out in order to compare the HIM to the more widely used technologies like SEM.

2.1 Introduction

Biological systems function at the nanoscale level. Cell membranes display nanoscale arrays of receptors and ligands, the cytosol is organized by nanoscale cytoskeletal networks, and nanoscale molecular motors form the primordial basis for motility at the micro- and macro-scales [HA05], [ASB+09], [AGLD10], [VGT+12]. Scanning electron microscopy (SEM) has been the traditional method used to image micro- and nanoscopic features on the surface of biological samples such as insect cuticles [WCW10], [DGMRSR12], [TCE12]. Advances in scanning particle beam microscopy and atomic force microscopy technologies have opened up surface science at the nanometer scale [KKE+11], [BARB12], [HVL+12], [VBFSHW12]. While most light

microscopes have diffraction-limited resolution at several hundred nanometers, modern electron microscopes resolve objects on the order of 1 nm. Pushing the limitations of particle beam microscopy is a relatively new technique called helium ion microscopy (HIM) which has sub-nanometer resolution [JG11], [BARB12], [VBFSHW12]. However complications arise with the imagining of biological samples which are composed of carbon based materials and often relies on elaborate preparation for the greatest resolution.

HIM is used here to characterize nanoscale surface structures on the cuticles of adult and larval *Drosophila melanogaster*. While operationally similar to SEM, HIM probes a surface with a beam of helium ions instead of electrons. The use of a helium ion beam provides several unique advantages. Due to the optional usage of the lower energy electron flood gun to neutralize the possible positive helium ion charging, HIM eliminates the need to use a sputter coating layer on the sample, thereby allowing imaging of biological samples in more of their natural state. This feature is particularly important for high resolution imagining of surface structures on biological samples [BARB12], [VBFSHW12]. Additionally, the mass of the helium ion produce a smaller interaction volume beneath the surface thus producing a restricted region generating the secondary electrons in biological materials [AKvVM12]. This permits imaging at high magnification without decreasing beam energy, resulting in higher resolution. The diversity of surfaces found on the cuticle of the fruit fly, *D. melanogaster*, are used here to demonstrate the discovery potential of HIM and compare it with existing scanning microscopy technologies.

2.2 Materials & Methods

The following strains of *D. melanogaster* were used in these experiments: Oregon-R strain was used as the wild-type control (*Bloomington Stock Center # 113*); *singed/sn*^{3} (*Bloomington Stock Center # 113*); *forked/f*^{36a} (*Bloomington Stock Center # 43*); *Moiré/Me*^{1} (*Bloomington Stock Center #594*); *roughex/rux*2 (*Bloomington stock #95*); *roughish/rh*^{1} (*Bloomington Stock # 385*); *shaven baby-sparkling/sv*$^{spa-1}$ (*Bloomington Stock # 638*); *roughest/rst*^{6} (*Bloomington stock # 1530*); *Rough eye/Re*^{1} (*Bloomington stock # 1845*); *lozenge/lzK* (*Bloomington stock # 2387*); *Epidermal growth factor receptor-elipse/Elp*^{1} (*Bloomington stock #2-153*); *Stubble/Sb1* (*Bloomington stock # 4938*); *rough/ro* (*Bloomington Stock # 569*); *roughoid/ru* (*Bloomington Stock Center #575*). All stocks were cultured on a standard cornmeal/molasses medium.

Adult *Drosophila* flies were reared at 20°C and on a standard cornmeal/molasses medium. Adult flies were collected for sample preparation three days after eclosure and euthanized by cold exposure, -20°C for ∼1h. The samples were fixed in a solution consisting of 2.5% gluteraldehyde (Ted Pella 18426) and 2% formaldehyde (Ted Pella 18505) in a 0.1M cacodylate buffer (pH 7.4) for ∼12h. Fixation ensured that the cuticle did not collapse during desiccation, presumably by crosslinking the underlying soft tissue. After fixation samples were washed six times in distilled water and dehydrated in an acetonitrile series (50%, 70%, 90%, 95% and 100%, twice). Once fixed and dehydrated, the specimens were mounted on EM mounting stubs (Ted Pella 16111) and were secured to the stub with double sided carbon tape. Prepared specimens were stored in a sealed desiccation chamber until imaging.

As a comparison with traditional particle beam microscopy and to demonstrate the resolution capabilities of helium ion microscopy, some samples were sputter coated with approximately a 30nm layer of gold (Pelco model 3 Sputter Coater 91000). When required, other samples were sputtered with a Leica EM ACE200 equipped with a quartz crystal microbalance to monitor layer thickness, and an angled rotating stage to ensure an even coating. Carbon coating was performed on the Leica EM ACE200 using a flat stage without rotation.

Soft tissue from larvae was dissected in a phosphate saline buffer solution, fixed in a solution consisting of 2.5% gluteraldehyde and 2% formaldehyde for 12h at 4∘C. Samples were dehydrated immediately in the acetonitrile series and then dried onto the SEM stub after treatment with a short incubation (less than 10min) with hexamethyldisilazane (HMDS) which has proven to be an excellent alternative to critical point drying with these samples [BBK93], [HCM12]. Long incubation (i.e. greater than 3h) of the sample with HMDS resulted in the polymerization of this material in and around the sample.

A Zeiss Orion Plus Helium Ion Microscope, Zeiss Auriga FIB/SEM, EVOLS10 Environmental SEM (Carl Zeiss, Oberkochen, Germany) were used to characterize the nanostructures found on the samples. Working distances for both HIM and SEM imagining were typically 4-10mm. Accelerating voltage was 25-35kV with the blanker current kept between 0.3 and 1pA for the HIM, and less than 1kV for uncoated samples in the SEM. For the EVOLS10 the accelerating voltage was 15kV and performed under extended pressure mode at 70Pa to account for charging of non-coated samples. During HIM imaging, the current was controlled by changing helium gas pressure, spot size, and/or aperture size.

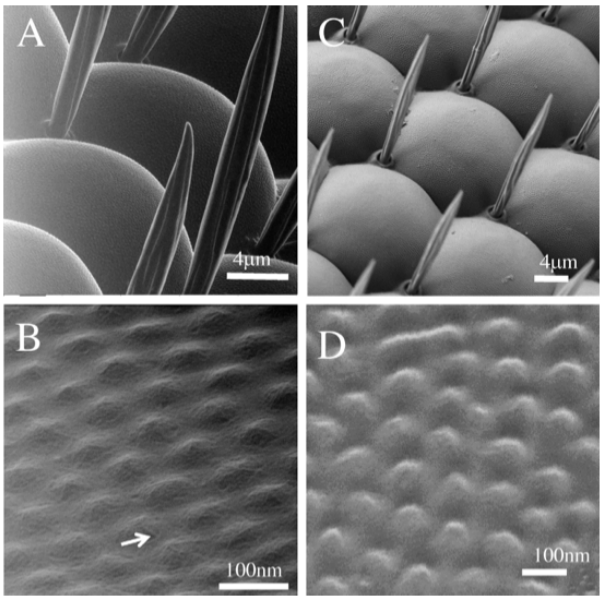

Figure 5. HIM and SEM Images of Corneal Nipple Arrays. (A and B) Native surface of the adult wild type ommatidia imaged using HIM. Scale bars A, 4μm; B, 100nm. (C and D) SEM native surface of wild type adult eyes, Scale bars A, 4μm; B, 100nm. (B) At the highest magnification ∼200,000x, under HIM the nanotextured surface of the ommatidia appears to contain fine fibers (arrow), while a SEM image at lower magnification ∼50,000x resolves fewer details other than the conical nipples.

The HIM uses also an electron flood gun, which produces a flow of low-energy electrons to a specified area on the sample, to neutralize charging. The location of flood gun target was specified by adjusting the x- and y-coordinates of the gun manually and the signal increased empirically by tilting the stage toward the flood gun.

2.3 Results

The *Drosophila* eye is composed of 800 optical subunits called ommatidia; the surface of each ommatidia is decorated with an array of conical nanostructures called corneal nipples [Gem66], [KKE$^+$11]. Standard SEM has been also been used to image uncoated samples by using a field emission gun along with a lower energy electron

beam [BJ96], [MRM$^+$05], [TCE12]. We compared the image resolution of HIM to SEM by imaging the uncoated surface of the eye on adult *D. melanogaster*. At lower magnifications, both HIM and SEM reveal the presences of these arrayed nanostructures (Fig. 5A and C); however, at extremely high magnification only the HIM provides a detailed surface image of the corneal nanostructures (Fig. 5B compared to D). At this level of resolution, incredible details can be observed, including the fine, fibrous material between 10 and 20nm, on the surface (arrow, Fig. 5B). In these experiments, the corneal nanostructures were measured using the measure feature in the software to be 140 $\pm$ 35nm wide and are spaced 220 $\pm$ 60nm center to center, which fit strongly with previous studies and the dimensions of the corneal nipples as determined by HIM also matched measurements that were independently verified using atomic force microscopy [Gem66], [KKE$^+$11]. These results demonstrate the HIM allows for both imaging and characterization of the dimensions of nanoscale structures on uncoated biological material.

To further test the HIM, we examined the eyes of mutant flies for previously characterized genes that affect eye morphology. We wanted to determine whether they also affect eye organization of the corneal nipples. We examined eleven different genes (see Section 2.2). The genes associated with these mutations have been molecularly characterized and are involved in many cellular process including signal transduction, proteolysis, apoptosis, and cytoskeletal. Many of these genes are required for multiple steps during eye development, but also function in later roles during the maturation and terminal differentiation of cells and structures in the eye [TGCZ94], [WUF00], [Car07], [Kum12].

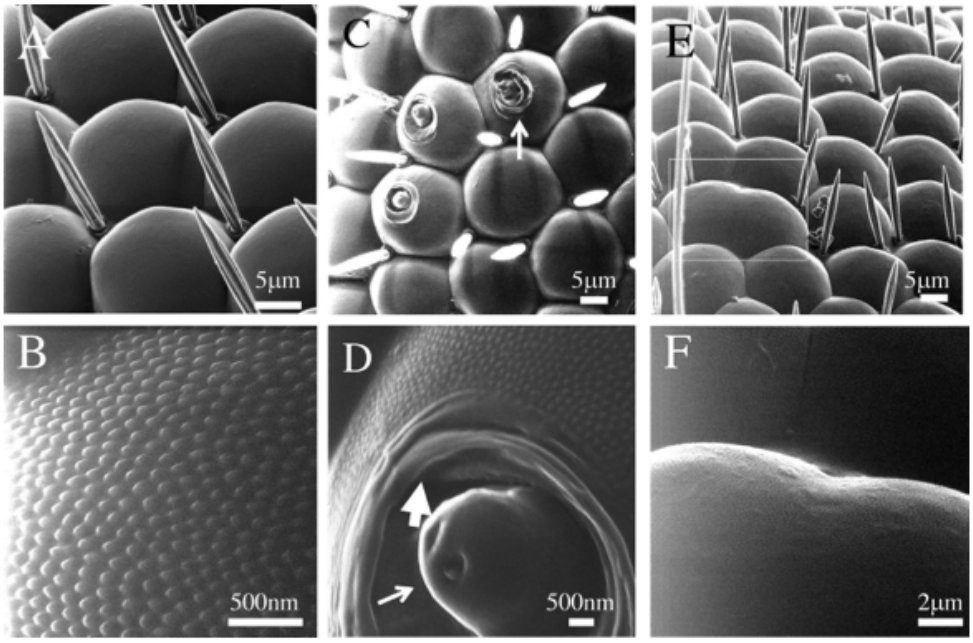

Figure 6. HIM Images of Mutant *D. melanogaster* Eyes. (A and B) HIM native surface of the adult wild type ommatidia. Scale bars A, 4μm, B, 500nm. (C and D) *Roughoid* mutant eyes. Scale bars C, 5μm and D 500nm. (C) Notice that not all of the ommatidia have the disrupted morphology. (D) At higher magnification the tissue does appear to be bristle like (thin arrow) and the area around the disruption is smooth lacking any nanotexture (thick arrow). (E and F) HIM image of an eye from a *roughest* mutant fly; (E) fused ommatidia can be observed (white box), (F) but there is no alteration to the pattern of corneal nanostructures over the surface; Scale bars A, 5μm, b, 2μm.

As expected, when viewed at low magnification all fly eyes examined show striking alterations to their general ommatidial organization (Compare Fig. 6A-C and E, Supplemental Fig. 2, which is often characterized by fusion of the ommatidia (see box in Fig. 6C) and morphological changes of the ommatidia (See arrow, Fig. 6C). At higher magnification, we observed subtle alteration to corneal nipples and other finer surface features of the eye in only one rough eye mutant, *roughoid* (*ru*) (Compare Fig. 6B, the wild type control to Fig. 6D, *ru*).

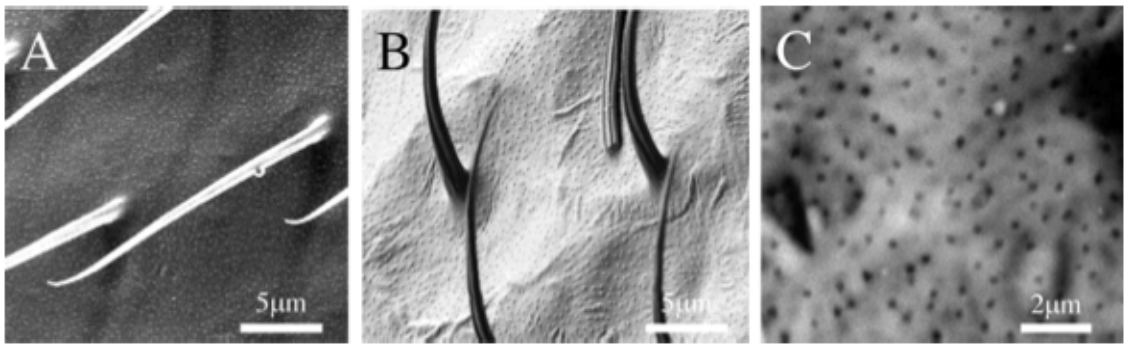

Figure 7. HIM and SEM of *Drosophila* Wing Nanostructures. (A) HIM image of a wild type *Drosophila* uncoated wing surfaces is covered with an array of regularly spaced wing hairs, the surface of the wing below is covered with small disorganized arrays of nipples. Scale bars, 5μm. (B) SEM image of a wild type *Drosophila* uncoated wing, the same small disorganized arrays of nipples are visible below the hairs. Scale bar, 5μm. (C) Higher magnification image of the wing, the nipples appear darker (thin arrow) than the surrounding non-nippled surface due to the charging of the thinner non-nanotextured area. Scale bar, 2μm.

Adult flies homozygous for a *ru* mutation expressed alteration to the surface organization of the ommatidia characterized by disruption of the center portion of some ommatidia (2-3%), but not all (Fig. 6B). The tissue erupting from the center of the affected ommatidia resembles a bristle (Fig. 6D, arrow) and the peripheral area surrounding the eruption is smooth and devoid of any nanotexture (Fig. 6D, thick arrow). We observed no alteration to the corneal surface in any other rough eye mutants despite microscale abnormalities such as the fused ommatidia found in roughest mutant eyes (Fig. 6E and F).

Wing and body surfaces of adult *Drosophila* were examined to determine whether these surfaces also have nanotextures. The dorsal and the ventral wing surfaces of Drosophila are covered with an array of fine wing hairs (700nm; Supplemental Fig. 4A) with each cell in the wing secreting a single hair [ACP94], [RHS$^+$06]. Like with the

eye we compared the resolving ability of the HIM with the images from SEM using a lower energy beam and found that we could easily resolve the wing nipples using either technique (Fig. 7A, HIM, and B, SEM). Both surfaces of the wings are decorated with small nanostructures (120 ± 30nm wide) resembling the corneal nipples with much less order. We were unable to resolve these structures at higher magnification using the HIM due to the charging of the wing which resulted in a negative image of these nipples (Fig. 7C). Unlike the closed-packed ordered nanostructures on the wings of cicadas and the corneal nipples on the eyes of *Drosophila* and moths, the adult *Drosophila* body and wing nanostructures are not closed packed and have little organization. Conical nanostructures were also found on the thorax of the adult fly (Supplemental Fig. 2B). Both the body nipples and the wing nipples are the same size (130 ± 30nm). We have found that coating the sample with a thin layer of gold (30nm) allows better resolution of the organization of these structures (Supplemental Fig. 1C), but prevented a detailed characterization of the native surface (Supplemental Fig. 1C, inset).

The cuticle of *D. melanogaster* contains sensory organs that are manifested as bristles; large macrocheates found predominantly on the dorsal mesothorax of the adult fly and smaller microchaetes which are found throughout the cuticle [GG92], [FHA02]. Bristles are components of the insect nervous system and the bristle's structural properties are generated as a direct extension of the actin cytoskeleton in the bristle cell [FHA02], [GCR$^+$03]. During the course of bristle morphogenesis, actin filaments are organized into the cellular projection of the presumptive bristle; these cables of actin are then organized into seven or eight distinct bundles [Ove67], [CKMC94], [FHA02], [TCR$^+$03].

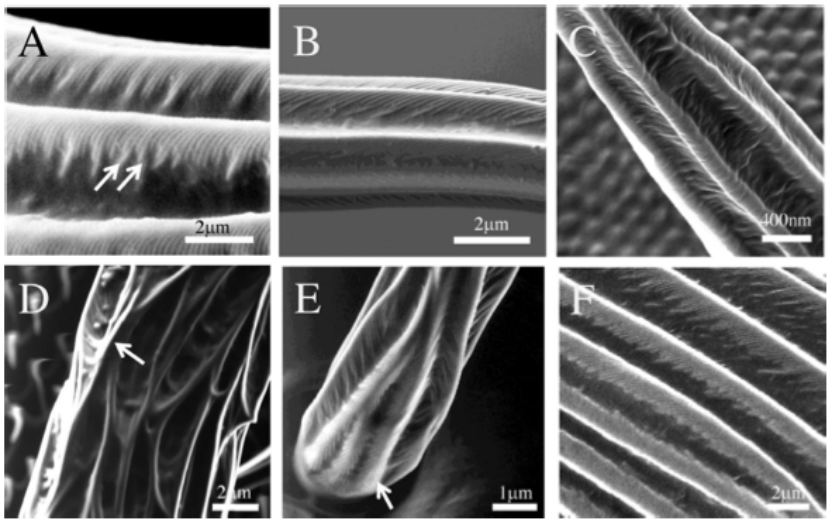

Figure 8. HIM and SEM of Bristle Nanoribs in Wild-type and Mutants. (A) HIM image of the surface of the bristle ridges that are textured by nanoribs (55nm wide). Scale bar, 2μm. (B) SEM image of the bristle surface also showing the nanoribs. Scale bar, 2μm. (C) HIM image of a gold coated bristle, the nanoscale ribs are no longer clearly present. Scale bar 400nm. (D) The nanoribbing that was a predominant feature of wild type macrochaetes is diminished on *sn* bristles and is only marginally apparent in clumps and fan-like arrays along some ridges (arrow); scale bar 2μm. (E) Although the ridges of *f* bristles resemble *sn* in general organization (Supplemental Fig. 5), the nano-ribbing along the bristle ridges is more prominent than in wild type although the size and pattern is generally the same. Scale bar 1μm. (F) *Sb* bristles have the nanoribs along the length of the ridges although they appear thinner (arrows). Notice the increase in the number of ridges in the field of view as another indication of increase in ridge number, Size bar, 2μm.

We examined the surface of bristles using HIM and SEM and observed two orders of structural organization. At the micrometer scale, each bristle possesses longitudinal ridges (1.2 $\pm$ 0.1μm) that span its length (Fig. 8A, arrow). At the nanometer scale, we found that each longitudinal ridge has nanoscale ribs that are 55 $\pm$ 15nm wide and offset to the length of the bristle (Fig. 8A, arrows). These nanoribbed structures were also resolved by SEM (Fig. 8B), but were completely obscured when the samples were sputtered coated with a layer of gold (Fig. 8D).

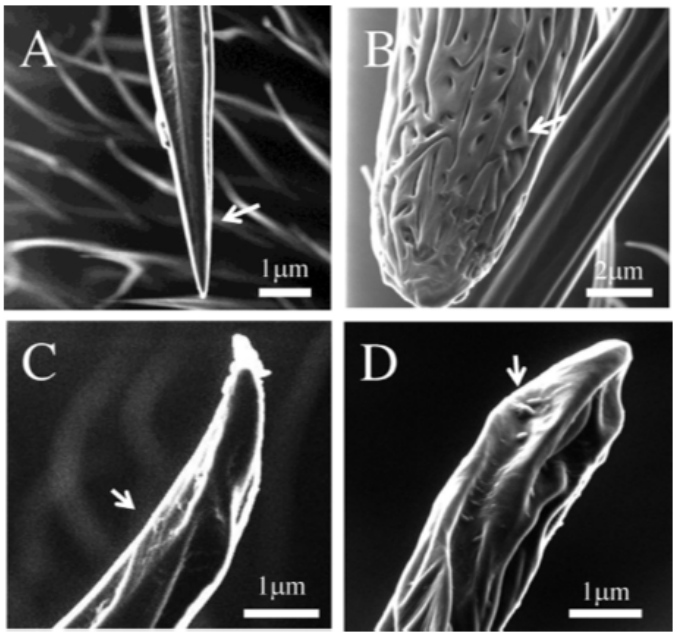

Figure 9. HIM and SEM Images of Bristle Tip Morphology. (A) HIM image of wild type bristles showing that the tip of the wild type macrochaete tapers to a fine point, proximal to this point (arrow head) the fine ribbing between the ridges can be seen to connect (fine arrow). Scale bar, 1μm. (B) The tip of a *Sb* bristle is filled with pores (arrow). Nanoribs are visible on the surface of the bristle but a few are perpendicular to the direction of the longitudinal fiber and none of the longitudinal ridges merge into a smooth taper like the wild type bristle in (A). Scale bar 2μm. (C) The tips of *sn* bristles coalesce into a blunt tip (arrow), Scale bar 1μm. (D) The tip of *f* bristles are blunt like *sn* tips, clumps of bristle material also accumulate at the tip (arrow). Scale bar 1μm.

This may provide some rationale as to why these nanoscale structures have not been previously reported.

We examined the bristle morphology of mutations in genes that are required for proper bristle morphogenesis: *stubble* (*Sb*), *singed* (*sn*) and *forked* (*f*). *Sb* is a dominant mutation that expresses short and thick bristle phenotype (Supplemental Fig. 5B). Flies homozygous for *sn* (Supplemental Fig. 5C), and *f* (Supplemental Fig. 5D)

have twisted and kinked bristles. At high magnification *sn* bristles have irregular longitudinal ridges of different lengths and that are separated by valleys of different depths (Fig. 8D). The nanoribs prominent in wild type flies are reduced along the longitudinal ridges and when present are often irregularly arrayed in a fan-like manner (Fig. 8D, thin arrow). Although morphologically similar to *sn* bristles, *f* mutant bristles have the nanorib structures (Fig. 8E, arrow). Although *Sb* bristles have more longitudinal ridges than wild type (Overton, 1967), the nanoribs appear similar to wild type (Fig. 8E). We also examined the tips of bristles in wild type and bristle mutant flies. The tip of a wild type bristle tapers neatly to a point (100 nm wide) (Fig. 9A, thin arrow). The morphology of the tips of *Sb* bristles differ radically from wild type; *Sb* tips have pores along the thin ridges (Fig. 9B arrow), furthermore, the longitudinal ridges twist and fuse in irregular ways at the tip. Previous characterization of *Sb* showed that the fiber bundles are thinner than the wild type bristles and are in a greater number than in developing wild type bristles [Ove67]. The tip of the *sn* mutant bristle is curved and comes to a blunt point and the ridges, when they meet, are smooth (Fig. 9C, arrow). The tip organization of *f* mutant bristles is similar to *sn*; it is irregular, having a twisted and rounded-off appearance of the longitudinal fibers and clumps of material are present near the tip (Fig. 9D, arrow).

The *Drosophila* tarsus is an elaborate structure most notably consisting of a centrally located empodium (big arrow head) that is flanked dorso-laterally by two tarsal claws (Fig. 10A, thick arrows) and ventrally by two sets of hairy type pulvilli (Fig. 10A one pulivillus, thin arrows). The pulvillus contains filamentous structures called setae that function to generate increased surface area and facilitate adhesion.

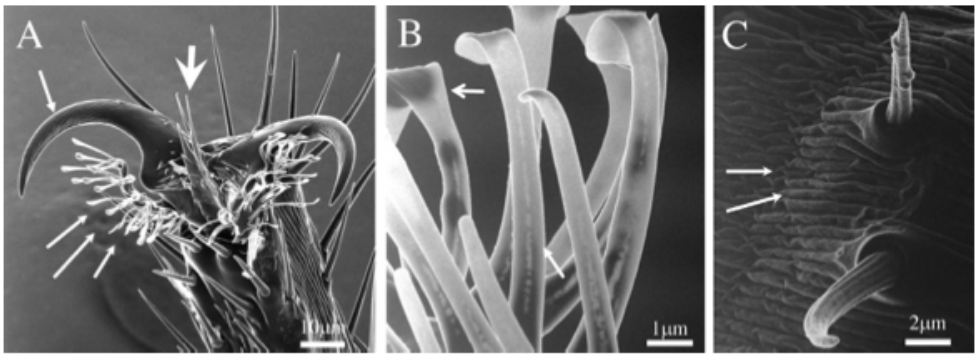

Figure 10. HIM Micrographs of the *Drosophila melanogaster* Tarsus. (A) Ventral view of the *Drosophila* tarsus, with the empodium (big arrowhead) that is flanked dorso-laterally by two tarsal claws and ventrally by two sets of pulvilli. Scale bar, 10μm. (B) Dorsal view of the pulvillis. Note the slightly grooved surface of the face of the setae (thin arrow) and the channel-like structure along the length of the filament (arrow). Scale bar, 1μm. (C) Dorsal epicuticle of the tarsal segment, note the grooved surface (arrows). Scale bar, 2 μm.

Each seta is a blunt structure with a slightly cupped, grooved surface (Fig. 10B, open arrow) and a channel-like structure along its length (Fig. 10B, closed arrow). The dorsal surface of the tarsus is covered by bristles with a wrinkled epicuticle and a system of valleys and ridges (475 $\pm$ 100nm) that travel the length of the appendage (Fig. 10C, arrow).

The *Drosophila* pupal case or puparium is the hardened cuticle layer that is derived from the larval cuticle and serves as the incubator for the metamorphosis of adult fly from the larvae [TSC$^+$08]. The anterior end of the cuticle is marked by the presence of two anterior spiracles (Fig. 11A, arrow) and the operculum (Fig. 11A, asterisk), which is the section of the puparium that opens and allows the eclosing emergent adult fly to leave the case for metamorphosis. At higher magnification the anterior spiracles appear finger-like with a rough scale like texture and a smoother rounded tip which serves as the opening to the atmosphere (Fig. 11B).

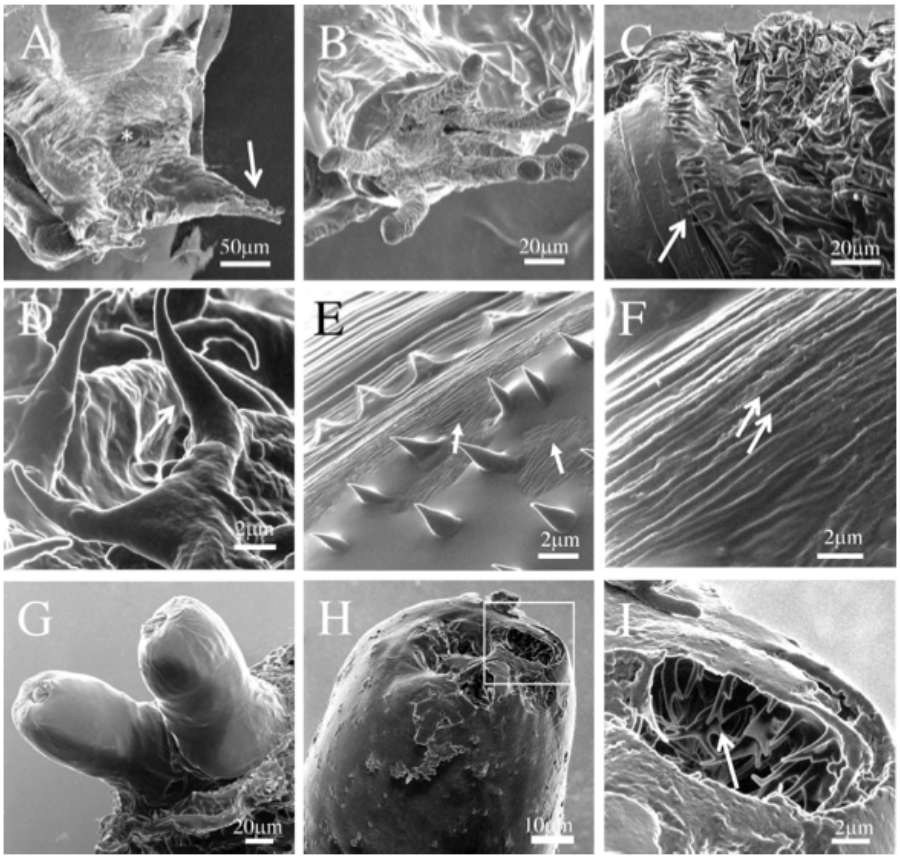

Figure 11. HIM Images of *D. melanogaster* Puparium Nanomorphology. (A) Ventral view of the anterior portion of the puparium (arrows) and the operculum (asterisk). Scale bar, 50μm. (B) At higher magnification the anterior spiracles appear fingerlike with a rough scale like texture and a smoother rounded tip which serves as the opening to the atmosphere (arrow). Scale bar, 20μm. (C) The surface of the puparium is composed of bands of material, some fibrous and others smooth (thin arrow). At regular intervals there are banded regions within the puparium which have tooth-like structures, called denticles, jutting from the surface (thick arrows). Scale bar, 20μm. (D) Close up of denticles (arrow). Scale bar, 2μm. (E). Denticles vary in size and shape (thick arrows) depending on their location within the cuticle; more fibrous layer can be seen adjacent to the denticles (fine arrows). Scale bar, 2μm. (F). The fibrous layer is composed of fibrous bands around the circumference of the puparium (arrows), Scale bars, 2μm. (G) At the posterior end of the puparium are the posterior spiracles. Scale bar 20μm. (H) These structures are hollow, look at box, and (I) filled with a fibrous network composed of fibers that are 340 $\pm$ 130nm wide (arrow). Scale bars 10μm for H and 2μm for I.

The surface of the puparium is composed of bands of material, some fibrous and others smooth (Fig. 11C). At regular intervals there are banded regions within the puparium that have tooth-like structures, called denticles that jut from the surface cuticle (Fig. 11C, arrow, close up Fig. 11D, arrow). The denticles vary in size and shape depending on their location within the cuticle (Fig. 11D and E). Furthermore, the surface surrounding these structures often appears smooth although a deeper, more fibrous, layer can be seen adjacent to the denticles (Fig. 11E, arrows) suggesting a superficial layer of wax may accumulate around these projections. The fibrous layer is composed of bundles (150 $\pm$ 40nm wide) that wrap around the circumference of the puparium (Fig. 11F, arrows). At the posterior end of the puparium there are posterior spiracles (Fig. 11G). These structures are hollow and filled with a fibrous network composed of 340 $\pm$ 130nm wide fibers (Fig. 11H and I, arrow).

The previous cuticle samples had several factors which facilitated imaging them with a particle beam microscope; foremost, they were hard and even in their native state contained little water which allows for little alteration after dehydration and drying. To determine whether HIM can image soft tissues we examined the soft cuticle and the midgut of the larvae of *D. melanogaster*. Soft larval cuticle has a higher water content than the adult hard cuticle, and is flexible, until it forms the hard cuticle of the adult exoskeleton [Wig85], [KS11]. To examine the larval cuticle, we prepare samples using a modified preparation protocol which included the addition of a hexamethyldisilazane drying step after dehydration to preserve the anatomical and cellular structure. Imaging the larval cuticle we observed numerous nanoscale pores on the larval head region (Fig. 12A and D thin arrows) and denticle structure (Fig. 12A and B, black box).

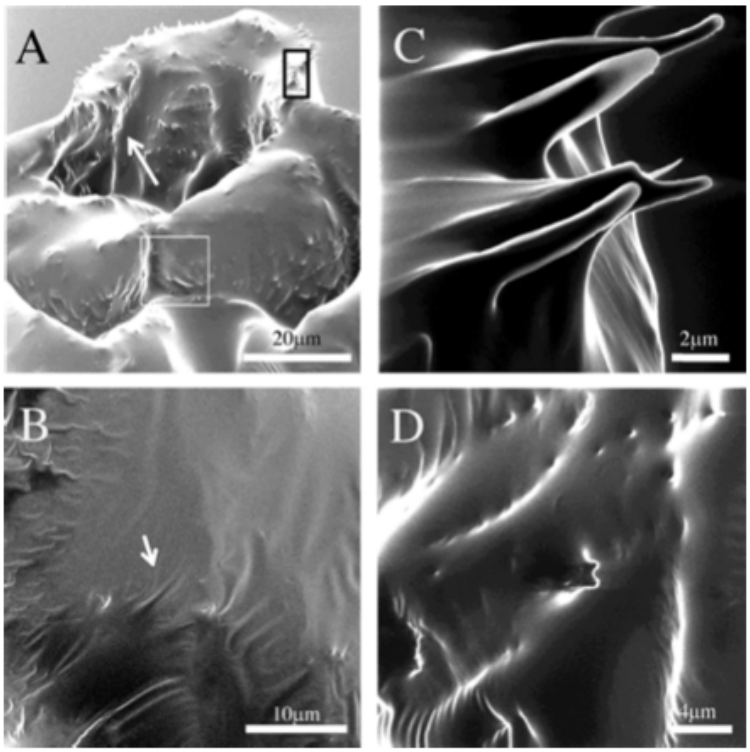

Figure 12. HIM Images of Larval Soft Cuticle. (A) Image of the anterior (head) region of a third instar larva. The surface is marked by pores (arrows), anterior denticles (black box) and ruffled cuticle. Scale bar, 20μm. (B) Higher magnification of ruffled cuticle on the larva. Scale bar, 10μm. (C) Higher magnification of the anterior denticles. Scale bar, 2μm. (D) Higher magnification of cuticle pore 200 nm in size. Scale bar, 4μm.

The cuticle surface was smooth except at the junction of larger features (Fig. 12A, white box) such as a fold or bend in a larval segment, where the cuticle is wavy and rippled (Fig. 12B, arrow).

We also examined non-cuticle tissues using HIM. For these experiment we prepared the tissue samples in the similar manner to the soft cuticle. The larval midgut is a tube that is composed of several layers.

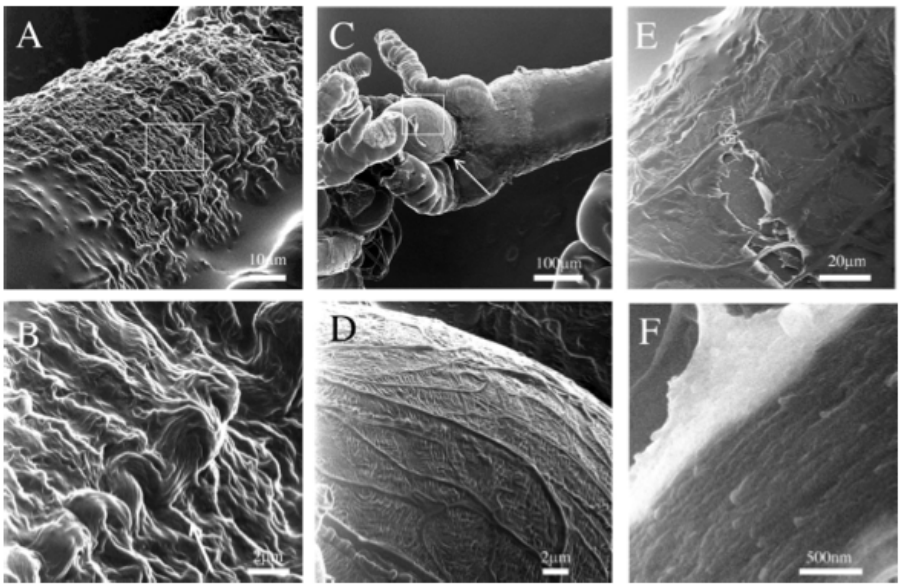

Figure 13. HIM Images of the Larval Midgut. (A) Low magnification HIM image of the visceral midgut, the checkerboard pattern is generated by the underlying visceral musculature. Scale bar, 10μm. (B) High magnification HIM image of a longitudinal visceral muscle (arrow). Scale bar, 2μm. (C) Low magnification HIM image of the cardia/proventricular region of the larval midgut, white box is imaged at a higher magnification in (D). Scale bar, 100μm. (D) High magnification of the cardia/proventricular region of the midgut, the vermiform pattern is created by the large number of tertiary trachea in this region. Scale bar, 2μm. (E) Low magnification image of a torn midgut that exposes the underlying musculature. Scale bar 20μm. (F) High magnification of a torn muscle (white box in E), showing the striated pattern of muscle fibers. Scale bar, 500 nm.

An outer connective tissue layer contains tracheal tissue, two visceral muscle groups, an outer set of longitudinal muscles and deeper circular muscle group, and the interior endothelial absorptive epithelial layer [LJP$^+$10]. Even though the sample lacks any structural components such as chitin, the fixation protocol that we used preserved the overall morphology clearly presenting a non-collapsed tube (Fig. 13A and C). Although the superficial layer of connective tissue was not removed, the organization of the underlying visceral musculature is clear and appears as a checker-board pattern

at lower magnification (Fig. 13A). At higher magnification (Fig. 13B, the boxed region in A), the HIM clearly showed the longitudinal muscles to have a filamentous nature which is characteristic of their less organized sarcomere [LJP$^+$10]. We also examined the cardia or proventricular, region of the midgut (Fig. 13C). This bulbous structure (Fig. 13C, arrow) is located at the junction of the foregut with the anterior midgut and is composed of several layers of muscle. Again the checkerboard pattern of these muscles can clearly be seen. At higher magnification, the complex network of tertiary tracheal branches can be seen over the surface (Fig. 13D, boxed in C). These vermiform tubal structures range in size from 0.5 to 1.5μm and are composed of a single cylindrical cell that delivers air to the surface of the gut. We also examined the organization of the visceral muscle using HIM. The circular visceral muscles are composed of rings of two thin muscle cells (70μm wide 100μm long and 5μm deep) that are paired down the length of the midgut [LJP$^+$10]. During dissection these thin muscles often tear (Fig. 13E). The torn muscle under high magnification contained numerous filamentous structures that were between 50 and 800nm wide (Fig. 13F, arrow).

2.4 Discussion

Recently HIM has been used to study the collagen fiber organization of uncoated bone and the surface characteristics of the photonic scales on blue winged butterflies [BARB12], [TCE12], [VBFSHW12]. One of the proposed advantages of HIM is ultra-high resolution imaging of biological materials without a metallic coating. Metallic coatings are used to negate surface charging generated when imaging non-conductive materials. Although much effort has been spent to minimize the artifacts associated

with metal coating of samples, such as decreasing the size of the metal particles and limiting the thickness, [CCVB95], [Sch11], the drawback to metallic sample coating is that the additional surface layer has its own structure which can obscure fine nanometer scale structures and structures with high aspect ratios can be distorted by such coating . Uneven coating has also been shown to form image artifacts such as self-shadowing and clumping [Pre11], [BARB12].

While scanning particle beam microscope techniques such as environmental SEM have been developed that preclude the need for metal coating, the resolving power of these microscopes fall below that of standard SEM [MRM$^+$05], [TCE12]. Classic SEM can also be used to image uncoated samples through the use of lower beam voltages, but we have found that HIM provides several advantages over standard SEM for the imaging of uncoated samples. Foremost is the increase in absolute resolving power of nanoscale objects. This was most markedly clear in the analysis of the corneal nanostructures found on the ommatidia. The fine 5-10nm filamentous textures could be observed with HIM (Fig. 5B), while SEM imaging at even lower magnification revealed a less distinct surface (Fig. 5D). An increased depth of field is another advantage of HIM over SEM. At all magnifications the HIM showed a remarkable depth of field; HIM produced beautiful images of the pulvilli on the *Drosophila* tarsus showing multiple setae filaments in focus simultaneously (Fig. 10A and B). This extended depth of field is also clear in images of the larval midgut, where features can be discerned across the entire field of view on slanted and rounded surfaces (Fig. 13A and D).

Imaging with the HIM also has certain idiosyncrasies, thin samples tended to charge more readily than with SEM. In some cases this permitted the revelation of

different structures within the sample based on the different thickness within a sample. The pulvilli of *D. melanogaster* consist of broad and flat setae that have some texture (arrow, Fig. 10B), which suggests a wet-interface interaction. The source of the fluid for this adhesion has been demonstrated in the beetle to come from the base of the setae and, in some cases, emerge from a pore at ventral side of the endplate of a hollow setae [HG12] [Gor98]. The source of the adhesive emulsion in *D. melanogaster* has not been established, but the differential charging by HIM of the fine structure of the setae clearly showed a thin groove or channel along the longitudinal axis of the setae extending from the base to the cupped, wedged shaped tip (Fig. 10B, thin arrow) which could serve as the conduit for an adhesive emulsion.

Although HIM showed some advantages over SEM in certain situations, in some examples there was little or no advantage of HIM. Nanoscale structures such as the nipples found on the thorax and wing were clearly shown in both (Fig. 7). The nanoribs of the thoracic macrochaetes were also clearly identified by both (Fig. 8). Regarding the time it takes to obtain a high resolution image on our microscopes, SEM is faster than HIM. It takes longer to get a high resolution image with the HIM due to the extra time necessary for the flood gun to be properly adjusted. However, when compared to environmental SEM (ESEM) a relatively new methods that permits imagining uncoated, hydrated samples under pressure [MRM$^+$05], [TCE12], both HIM and uncoated SEM have a distinct advantage in the resolution of nanoscale cuticle structures and the depth of field (Supplemental Fig. 6). Although the nanoscale structures found on the eye and bristles can be observed by ESEM their organization is not as distinct as with HIM or uncoated SEM.

The *Drosophila* cuticle is a diverse structure that contains numerous microscale and nanoscale structures. In general, insect cuticle surface topology involves multiple levels of organization usually along two hierarchical orders: (1) microscale structures: pores, hairs, bristles, concave pits, scales, and grooves, and (2) nanoscale structures: nanopores, nanoribs, conical nipples, nanogrids, and irregular surface patterns which often decorate the surfaces of the microscale structures [BMM63], [SFPA06], [DKSM$^+$11], [KKE$^+$11]. The features found on the cuticle of *D. melanogaster* provide an ideal place to test the advantages of HIM.

We initiated our study by examining the compound eye of adult *D. melanogaster*. One of the advantages of using the *Drosophila* model system is the ability to characterize these structures using genetics. For the past thirty years, the *Drosophila* eye has been a model for tissue morphogenesis and has been extensively characterized genetically. We screened through a collection of eleven genes that when mutated resulted in a rough or malformed eye. Only one of these genes, *roughoid* (*ru*), expressed a slight alteration to the corneal structure (Fig. 6C and D). Earlier characterization of *roughoid* mutant eyes described a weak rough eye phenotype that exhibited unknown material emanating from the occasional erupted facets, but did not elaborate on the material or eruption in any detail possibly due to the metallic surface coating and reduced resolution [STD74]. In this study we showed that a subset (2-3%) of *ru* ommatidia where malformed having a bristle-like structure erupting from a smooth nanotexture free surface.

In addition to observing the corneal nipples of the ommatidia, we found nipple-like conical nanostructures over the surface epicuticle of the wing and body of *D. melanogaster* (Fig. 7 and Supplemental Fig. 4). These structures differed in size and

distribution from the nipples found on the eye. Unlike the neatly arrayed corneal nipples, the body and wing nipples appeared to be disorganized and scattered across the surface of the wing and body. Body and wing nipples are broader than eye nipples, which is perhaps functionally significant.

The numerous sensory bristles and hairs decorating the surface of the adult fly provide the cuticle surface with a predominant microscale morphological landscape. There are two general categories of bristles: larger macrochaetes found on the dorsal mesothoracic surface of the adult fly and, more common, smaller microchaete and other bristle-like cellular protrusions are on the wing hairs and the lateral projections of the arista [TTG95], [FHA02]. Bristles and bristle-like structures function mainly as mechanical or chemical sensory organs and form from cellular extensions that contain bundled actin (typically seven to eleven bundles in the large thoracic macrocheates) and a center microtubular core [TCSG96], [FHA02], [TCR$^+$03]. In the adult thoracic macrocheates, the impact of the bundled actin scaffold that is just below the plasma membrane is realized as longitudinal ridges that span the length of the bristle. While the longitudinal ridges are readily visualized, we were also able to identify lateral nanoribs that transverse the longitudinal ridges, which are two orders of magnitude smaller (1.2μm versus 55nm) using both HIM and SEM, on uncoated bristles. Using HIM, We investigated the alteration to the ultrastructure of bristles mutant for *Stubble* (*Sb*), *singed* (*sn*), and *forked* (*f*). In our investigation we identified a new nanoscale structure along the longitudinal axis of the bristle ridges that we call nanoribs. Nanoribs were present in wild type, *f*, and *Sb* flies, but we observed a significant reduction in the number and organization of the nanoribs in *sn* mutant bristles. The *sn* gene encodes a *Drosophila* FASCIN homologue that is required for

the bundling of actin in the bristle [CKMC94]. The loss of *sn* disrupts the nanoribs resulting in a relatively smooth bristle that is nearly devoid of nanoribs. These nanoribs may represent epicuticular chitin/protein complexes secreted and assembled during bristle morphogenesis, or they may be the remnants of the actin scaffolding underlying the deposition of cuticle. It has been shown that *n* and *f* work cooperatively to properly bundled actin in the growing bristle, loss of either results in a kinked and short bristle [TTG95], [FHA02]. Interestingly, loss of *forked* appears to accentuate the presence of the nanoribs on the surface, perhaps further suggesting a connection between actin crosslinking in the developing bristle and the nanoribs formation during cuticle deposition.

The *D. melanogaster* tarsus is another well characterized insect/environment interactive surface. Arbored 'hairy' footpads exhibit a remarkable set of adhesive structures that have independently evolved multiple times in diverse lineages of lizards, spiders, and insects [Fed06], [BF09]. Footpad structures can be further divided into two categories based both on structure and mode of operation. Dry function footpads contained branched filaments or setae that utilize a surface adhesive system that does not require a fluid interface [Fed06], [DCF10]. Dry adhesive pads are most famously observed in the feet of geckos and have been successfully mimicked using synthetic materials [GSP$^+$07], [YDRGG08]. Wet adhesive footpads have setae that are unbranched and use lipid/aqueous emulsion to facilitate binding to a substrate, but also permit the rapid release of the foot from the surface [Fed06], [KFG13]. In addition to setae, the Drosophila tarsus has other nanostructures whose function remains unclear, but may be involved in roles other than locomotion such as chemical sensing or grooming.

We also used the HIM to examine the cuticle of the puparium and several examples of soft tissue: larval cuticle and the larval midgut. The puparium casing serves as the protective barrier for the developing metamorphosing pupa and is essentially the remnants of the larval skin [KDK$^+$03], [LD10]. The puparium prevents desiccation but must remain permeable to gas exchange. It is a natural composite material consisting of bands of 100-200nm fibers embedded in a waxy matrix. The structure of the casing appears hollow with the spaces perhaps representing the volume occupied by degenerated epidermal cells. Soft cuticles and tissue present a different set of challenges for imagining with particle beam microscopy. Being composed of materials that have a high water content, the process of sample preparation, particularly dehydration and the subsequent drying step, can alter the structure significantly; furthermore, the fragile nature of this type of sample also may preclude high energy/high resolution techniques. Using a relatively standard sample preparation, we showed that soft tissue samples can be prepared and image easily and to high detail. We imaged surfaces on the larval cuticle and on the larval midgut, identifying structures as small as 200nm pores and alterations to the larvae cuticle surface in the form of ruffling (Fig. 12B and D). Imaging the surface of soft tissues also proved to be also productive and opens the door for future work that examines and characterizes the surfaces of tissues and cells. HIM provides a powerful new tool for the characterization of the surfaces of biological samples at the nanoscale. With the resolution power down to the size of individual protein and/or molecular complexes, HIM in combination with other techniques like immunoelectron microscopy using nanogold conjugated antibodies may one day allow the characterization of the composition and nanoscale organization of complex biological structures.

CHAPTER III

BIOLOGICAL NANOSTRUCTURES

3.1 Introduction

Insects have been evolving and adapting to changes in their environment for millions of years. As a result, they've developed mechanisms to overcome many of the challenges threatening their survival. Some of these mechanisms can be found in the form of cuticular nanostructures. Here, we present some of these nanostructures and discuss their importance to the survival of the insects in which they are found.

Compound eyes of insects are made up of multiple subunits called ommatidia (Fig. 14). They contain various cells, including the photoreceptor cells, responsible for the insect's sight. Some ommatidia have been shown to contain a pattern of nanostructures on their surfaces that form a regular array of nipples (Fig. 14) [BM62]. Of these structures some have subsequently been shown to reduce the amount of light reflected from the eye [BGM68]. Also, there is evidence these structures perform additional functions like self cleaning [PG10]. More recently researchers have given novel properties, such as anti wetting and anti fogging, to materials by mimicking and performing theoretical modeling to tune the sizes of these features [PCC$^+$12]. This gives promise in looking to nature's nanostructures for help in improving our everyday lives.

For imaging biological substances with SEM, it is common practice to coat a sample with a thin layer (less than 50nm) of conductive material, typically gold or gold/palladium is used.

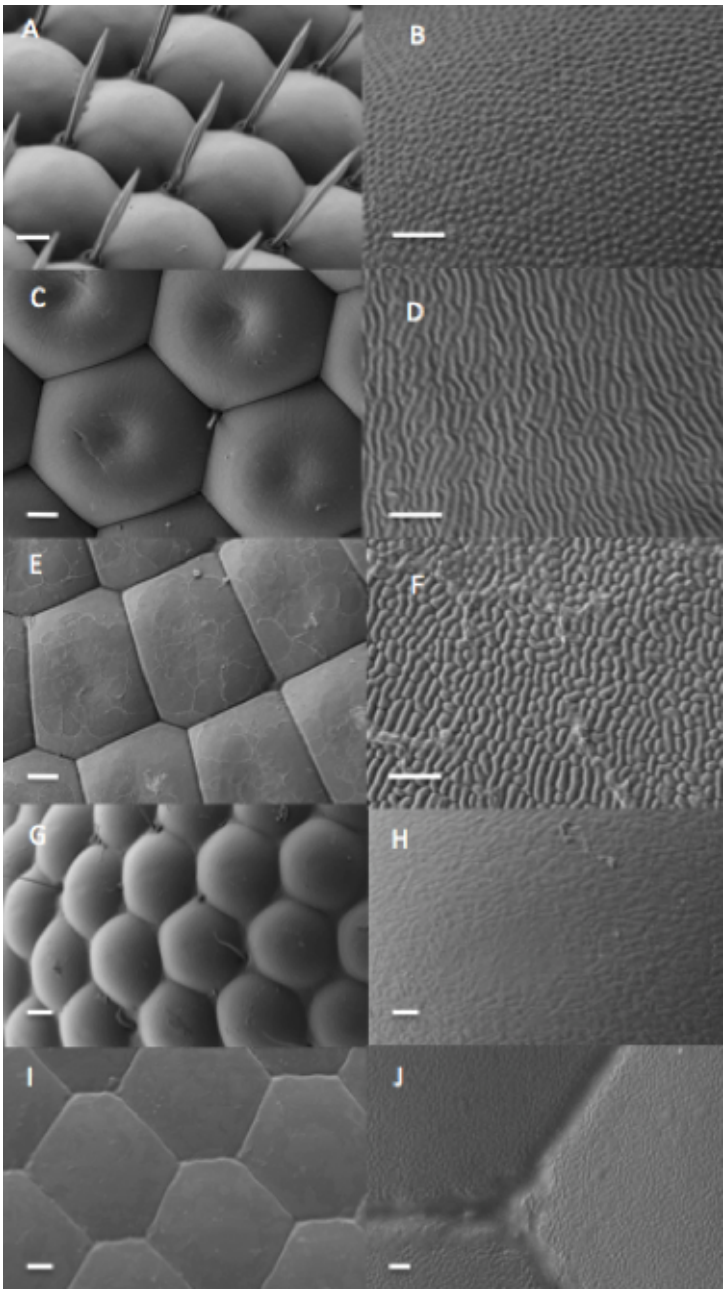

Figure 14. SEM Images of Various Insect Eyes. A,B) Fruit fly (*Drosophila*) Scale bars 4μm, 1μm. C,D) Horse fly (*Tabanidae*). Scale bars 8μm, 1μm. E,F) Robber fly (*Asilidae*). Scale bars 8μm, 1μm. G,H) Ant (*Formicidae*). Scale bars 5μm, 500nm. I,J) Hornet (*Vespa*). Scale bars 5μm, 1μm.

Features and details of objects are very important when analyzing an SEM image and even deposition of a thin layer of metal onto the surface can cover the finer features already present or create features from the metallization process. Leading to either omission of valuable data or observation of features that do not inherently exist. This begs the question as to why sputtering is so widely used for biological imaging when extra time, material, and equipment cost are needed for sputtering while it may not be necessary. To this end, no images shown in this study were sputter coated and none show the charging effects requiring sputter coating in the first place. In order to avoid the typical charging effects associated with imaging uncoated biological samples, a low accelerating voltage combined with a low working distance are needed. We are not saying that sputter coating is unnecessary, there are times when it is completely needed to coat a sample. Our goal here is to point out the common misconception that sputter coating is always required to image biological substances.

3.2 Materials & Methods

Insects used for comparison samples in this study were the fruit fly (*Drosophila melanogaster*), horse fly (*Tabanidae*), robber fly (*Asilidae*), hornet (*Vespa*), and an ant (*Formicidae*). Fruit flies are raised in our lab and the wild-type Oregon-R strain was used for imaging (Bloomington Stock Center # 113). All other insects were collected in the general area surrounding the university, resulting in a limited number of samples and undetermined species.

Fruit flies were reared at 20°C on a cornmeal/molasses medium, then collected for sample preparation three days after eclosure and euthanized by cold exposure at -20°C for 1 hour. All other insects were either found deceased or euthanized by

cold exposure upon collection. We prefer a widely used electron microscopy fixative consisting gluteraldehyde (GA) and formaldehyde (Form). The fixative is prepared by mixing 5 ml of 2.5% GA (Ted Pella 18426) with 10 ml of 2% Form (Ted Pella 18505) and 25 ml of 0.2M cacodylate buffer then adding 10 ml of dH2O. This ensures the cuticle does not collapse during desiccation by cross linking soft tissue in the underlying cuticle. If not washed thoroughly before and after fixation, remnants of debris or a film from the fixative can be left on the surface. Dehydration is done in a series of solutions of acetonitrile and dH2O (25%, 50%, 75%, 95%, and 100%X2).

Samples used in this study were imaged with a Zeiss Auriga scanning electron microscope using the secondary electron detector. In order to ensure valid surface observations, none of the samples used were sputter coated with a thin metallic layer as is commonly done to make them conductive. Thus, images were acquired with low energy and a short working distance to avoid charging effects. Typically, under 1kV accelerating voltage and less than 4mm working distance were used.

3.3 Results

High resolution SEM images of uncoated insect cuticular nanostructures were obtained from a wide variety of insects. A number of different nanostructures were seen and characterized in this study. The ommatidia of all insects contained a pattern of nanostructures which differed for each insect. These patters were characterized as: nippled, grooved, a mixture of nippled and grooved, and two irregular vermiform patterns. Also, we show nanostructured patterns on the exoskeletons of two of the insects shown, namely the ant and hornet. These patterns formed a grooved and porous vermiform surface, respectively (Fig. 14).

Measurements on the nanopatterns in Fig. 14 were performed with images obtained from the SEM. At least ten measurements from different areas on the ommatidia were taken to get an average for our data. We found the nipples on the fruit fly eye to be 140±34nm in diameter spaced 59±30nm apart (Fig. 14.B). The grooves on the horse fly eye are roughly 112±40nm wide, spaced 83±43nm apart (Fig. 14.D). Features found on the mixed surface of the robber fly eye are somewhat bigger and more densely packed at 146±20nm wide, spaced 70±27nm apart. The nipple-like features on the robber fly eye vary in length, the elongated ones were 238±112nm, and the circular ones were found to be 156±37nm (Fig. 14.F). The vermiform features on the ant were 158±28nm wide, 497±453nm long and spaced 41±20nm apart (Fig. 14.H). The features on the hornet were similar to those on the ant, but less densely packed at 171±33nm wide, 356±264nm long and spaced 106±50nm apart (Fig. 14.J).

Similar measurements were made on the nanostructures found on exoskeletons of the ant and hornet seen in Fig. 15. Features on the porous hornet exoskeleton were found to be 273±134nm wide, spaced 144±52nm apart (Fig. 15.C). The grooves on the ant exoskeleton are 98±18nm wide, spaced 44±13nm apart (Fig. 15.D).

3.4 Discussion

The overall structure of an insect's compound eye is roughly the same when seen at low magnification. They share a close-packed set of hexagonally shaped ommatidia, with the total number differing greatly between species. However, at higher magnification there are patterns of nanostructures varying in shape, height, size, and distribution. The most widely characterized pattern is a conical array of nipples (Fig. 14.B). Not surprisingly, other families of insects possessing completely different pat-

terns of corneal nanostructures. Specifically, we see the horse fly (*Tabanidae*) has an intricately grooved, fingerprint-like, pattern (Fig. 14.D) and the robber fly (*Asilidae*) has a mix between the grooved pattern seen on the horse fly and the nippled pattern seen on the fruit fly (Fig. 14.F). We have also seen two irregular vermiform features on the ant (*Formicidae*) and hornet eyes (*Vespa*). Patterns similar to those seen on the robber fly have been found elsewhere such as in other flies [BGS70], some millipedes (*Penicillata*) [MSR07] and some moths [RW00]. Grooves like those on the horse fly have also been seen on some moths [MRS93].

The nippled pattern found on the eyes of fruit flies and many moth species have been well studied for some time in literature [BGS70]. Much effort has gone into testing the properties arising from nano patterned surfaces in order to determine the underlying role they play. Using this knowledge, artificial surfaces have been mimicked after their biological counterparts to give them similar properties [PCC$^+$12]. Stunningly, the other patterns mentioned in this study have not been widely used as a source for innovative surface properties. Considering the benefits gained from the nippled pattern, it is highly likely these patterns are responsible for a different set of novel properties which have yet to be unveiled. Therefore, it is necessary to test these other patterns and determine whether any of said properties are associated with them.

Additionally, we've shown benefits gained by imaging uncoated samples. Metallization can cause unwanted artifacts especially when looking at the nanoscale. This can result in smaller features being covered, and the creation of features that don't naturally exist on the surface. By imaging with a low accelerating voltage and working distance, sputter coating can be unnecessary.

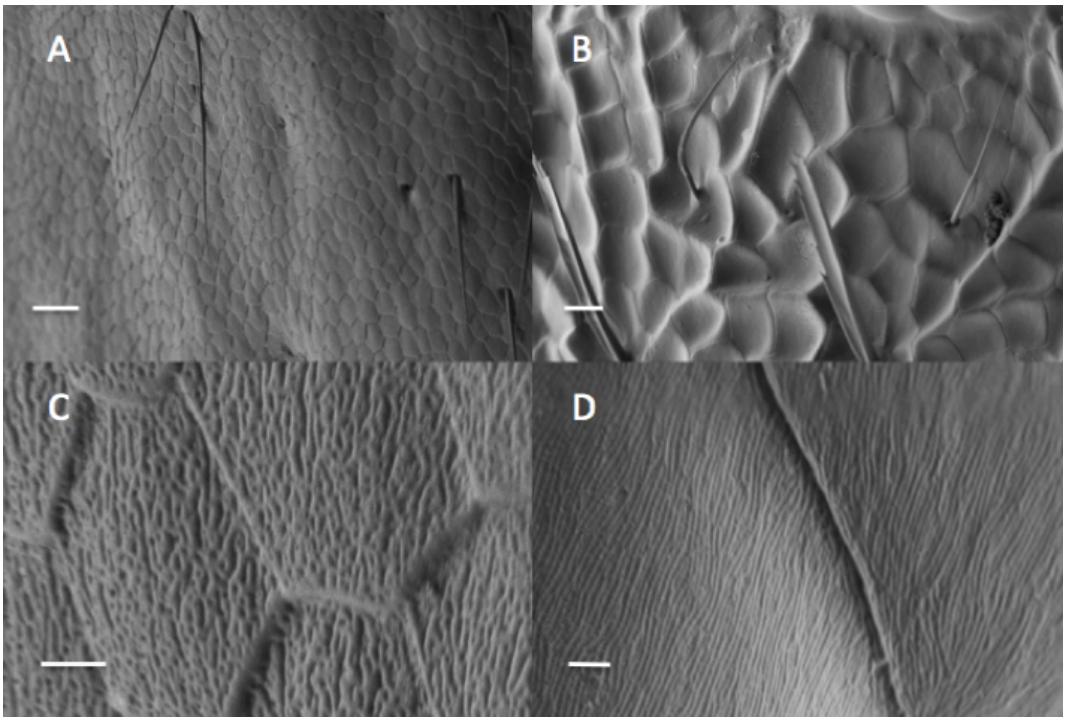

Figure 15. SEM Images of Various Insect Exoskeletons. A,C) Hornet (*Vespa*) with scale bars 20μm, 2μm. B,D) Ant (*Formicidae*) with scale bars 10μm, 1μm.

This is not to say sputter coating is always unnecessary though. Imaging soft tissue, for example, can still be challenging and may require sputter coating to avoid charging effects. We just hope to show that it is not always necessary to put in the extra time, expense, and equipment to get reliable SEM images from biological samples.

In this study, it was shown that sputter coating a biological sample may not always be needed when the proper imaging techniques are used. Also highlighted was the diversity of nanopatterns formed on the compound eyes of insects. Characterization of the nanostructured patterns found on five insects: fruit fly (*Drosophila*), horse fly (*Tabanidae*), robber fly (*Asilidae*), ant (*Formicidae*), and hornet (*Vespa*) has shown seven different nanopatterns. With this study, we are hoping to shed light on the

possible applications from the many different nanopatterns found in nature. It is likely these patterns will contain new properties in which modern materials can be created.

CHAPTER IV

BIOLOGICAL ADHESION

4.1 Introduction

The ability for some insect and gecko species to walk/run freely on smooth surfaces, even if vertical or inverted, has intrigued mankind for centuries. Many survival advantages are gained from sticking to a surface, especially when dealing with the incredible forces small insects must face. Something as simple as raindrops landing on the surface of a hanging leaf could be enough to trampoline a small ant onto the ground if it were not able to stick to the surface, leaving it lost and vulnerable to attack. Similarly, geckos living high in the treetops would need to be extremely careful of foot placement if they were not able to grip to, both the smooth and rough, surfaces of leaves branches. Adhesive traits have evolved over millions of years in nature to improve the ability of these animals to survive, and advances in modern technologies have provided us with tools to reveal some of the mechanisms behind these phenomena. We now know there are sets of pads on the feet of some insects, and toes of some geckos, responsible for this remarkable adhesion property. Pads found on geckos consist of many pillars with millions of tiny hair-like structures (Figure 16.A). Insects adhesive pads can be mostly broken into two classes, hairy or smooth, (Figure 16.B, C) [BG01]. The mechanisms behind their adhesion can also be broken into two classes: dry adhesion and wet adhesion. Geckos use dry adhesion which relies on van der Walls interactions [ASL$^+$02], while insects have been shown to use dry or wet adhesion [KMS04], [FRCF02].

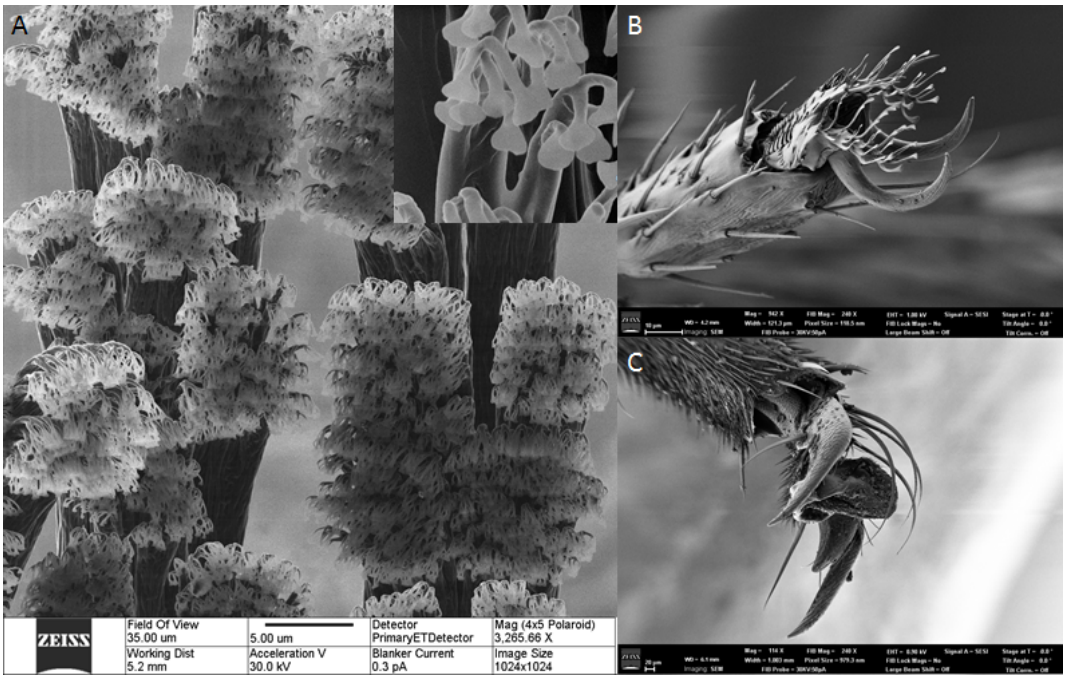

Figure 16. Gecko and Insect Adhesive Pads. A) Setae and spatulae on Tokay gecko (G.gecko) foot, spatulae are shown in the insert. Images courtesy Dr. Jijin Yang and Dr. Keller Autumn. B) Hairy-type on fruit fly (D.melanogaster). C) Smooth-type on honey bee (A.malifera). Structures of interest are between the claws in B, C.

Wet adhesion relies on capillary-mediated forces to increase the contact area on a rough surface [BF09]. Although there is an enormous amount of variety in shape and design of these systems found in nature, we will focus on just a few to emphasize key differences in function [BG01], [BG06].

4.2 Dry Adhesion

Dry adhesion is a trait found throughout nature in animals such as geckos and spiders which allows them to cling to seemingly any surface. When seen under low magnification, or with the naked eye, the foot of a Tokay gecko (G.gecko) has multiple rows of lamella (1-2mm) covering the underside of the toes and upon further mag-

nification each lamella is shown to have an array of stalks (setae) which branch off into 100-1000 tiny hairs with spatula-shaped tips called spatula (Figure 16.A) [KB07]. Spatulae are roughly 500nm X 200nm X 10nm [KB07] and have been shown to allow the gecko to stick to surfaces through van der Waals interactions [ASL$^+$02]. Named after a Dutch scientist Johannes Diderik van der Waal, these are intermolecular forces between molecules and surfaces including dipole-diploe, dipole-induced dipole, and London forces [Bra07]. The shape (iso- or anisotropic charging) and orientation of participating molecules are important for these interactions to occur. Intimate contact with a surface is required for these effects to take place. Three-level hierarchical structuring facilitates an increased contact area and maintains proper molecular orientation on rough surfaces, allowing geckos to walk freely on many different surface types [KB07]. Research has shown the adhesive force of a Tokay gecko's foot to be 10N, a single seta to be roughly 194μN, and estimates show a single spatula to be 0.4μN [ALH$^+$00]. Implying, if each spatula were optimally oriented and maximally attached a resulting adhesive force of 100N per foot is expected to be possible. Detachment obviously becomes an issue when dealing with an adhesive force, but by adjusting the contact angle of the setae geckos are able to lower the effective force and freely detach from the surface [ALH$^+$00]. Similar dry adhesion mechanisms have evolved in spiders that give them superior adhesion ability over insects, which require a thin layer of secreted liquid [KMS04]. Recent research suggests additional biological factors to be behind the mechanisms driving dry adhesion [GSG$^+$12] showing there is more work to be done before we have a full understanding of this phenomena.

4.3 Wet Adhesion

Insects use wet adhesion, which differs from dry adhesion in that it requires a thin film of liquid to stick onto surfaces. Fluid is released in a fashion similar to a sponge. Compression of the pad or capillary suction by contact with the surface causes a small release of fluid, while detaching the pad is decompressed and much of the fluid is reabsorbed into the pad [DF11]. Surface tension and viscosity are the mechanisms behind adhesion in the fluid film which has been shown to be a two-phase secretion that is mostly hydrophobic with small amounts of a highly volatile hydrophilic component forming drops between the hydrophobic portion (the hydrophilic portion is not always present depending on the surface) [FRCF02], [KMS04]. Another difference from dry adhesion is the number of diverse structures that facilitate adhesive forces in both hairy (fibrillar) and smooth pads [BG01], [BG06]. Fibrillar pads can take multiple forms including spatulate, discoidal, or pointed [BF11]. Each type has unique adhesion properties with discoidal having the highest adhesion force. Detachment is similar to what is seen with dry adhesion. Once the pad/setae have passed a critical surface contact angle, the forces are decreased allowing for the pad to be easily peeled away. There is still much work that needs to be done to uncover all the mechanisms behind the secretion process.

4.4 Discussion

Adhesives have long been utilized in different types of products like tapes, glues, and epoxies. A problem occurs when trying to remove something stuck by any of those adhesives. Most of the time either a sticky residue is left over, or the object is permanently stuck to the surface. Such issues can be avoided with the use of

dry adhesives. Recent advances in understanding and fabrication technology are now giving us the tools to recreate this phenomenon with amazing success. Bartlett et al. were able to fabricate a synthetic hand-sized adhesive pad that could hold around 2950N, or 660lbs [BCK$^+$12]. Remarkably, millions of years of evolution have given these structures many additional benefits. Along with controllable adhesion these structures have been shown to be able to adhere to rough surfaces and resist contamination in both dry and wet adhesion systems [BF11], [GSG$^+$12], [CBBF10].

CHAPTER V

BIODEVELOPMENT

5.1 Introduction

Applications derived from nanopatterned surfaces found in nature have brought many interesting abilities that may have once been thought of as fantasy into reality. Some of these applications include optics [KLK$^+$12], anti-wetting or anti-fogging surfaces [PCC$^+$12], dry adhesives [BCK$^+$12], and bactericidal surfaces [IHW$^+$12]. Although the methods used to realize these applications are quite interesting, it is still unclear as to how the natural structures are formed in the first place. A commonly used pattern scheme in nature is a nanoscale array of, what can be very intricate or basic, objects of varying shapes and sizes.

One example seen in nature that is very easy to study is found on the eye of the common fruit fly, *Drosophila Melanogaster* (Figure 17). The fruit fly is one of the most widely studies organisms due to its ease of handling in lab conditions. There is a great deal of work that has been done about the genetics of eye development, but none of this focuses on the formation of the nanopatterned surface found on the cornea even though it has been discovered for quite some time [BM62]. It is the goal of this study to determine when and possibly give insight into how these structures are developed. The eye of the adult fruit fly is composed of hundreds of small corneal lenses, called ommatidia, which can be seen in Figure 17.a. Each of these ommatidia are covered in a nanoscale array of approximately 100nm diameter hemispheres (Figure 17.b) [BNA$^+$13].

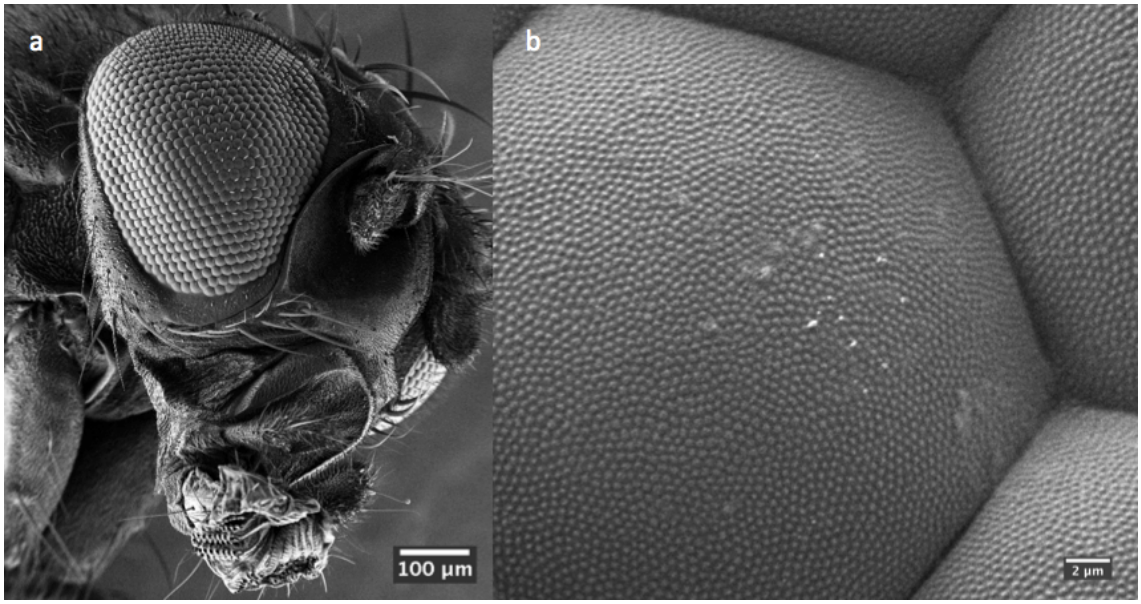

Figure 17. Adult *D. melanogaster*. a) Adult *D. melanogaster* head. b) Adult ommatidia showing fully formed corneal nanostructures.

These corneal nanostructures take on a semi-hexagonal pattern and cause an anti-reflective effect which has been shown in many other insects as well [BMM63]. The understanding of how these types of structures are formed naturally could lead to enormous breakthroughs in the way we produce materials today.

5.2 Materials & Methods

The wild-type *D. melanogaster* strain Oregon-R was used in this experiment (Bloomington Stock Center # 113). The stock was cultured on a standard corn-meal/sucrose medium at 20°C. When wandering third instar larvae stopped moving on the vial wall, they were given a unique symbol and the time and date was recorded. Developing pupae were collected during stages P5-P11 [CR89],[BB81].

Before fixation, the operculum was carefully removed to expose the developing head. Samples were fixed in a solution consisting of 2.5% gluteraldehyde (Ted Pella 18426) and 2% formaldehyde (Ted Pella 18505) in a 0.1M cacodylate buffer (pH 7.4) for at least two hours. After fixation, samples were washed three times in distilled water and dehydrated in an acetonitrile series (50%, 70%, 90%, 95%, and 100% twice). The head was removed after fixation and dehydration when possible, otherwise a portion of membrane covering the eye was removed. Specimens were then mounted on EM mounting stubs (Ted Pella 16111) and stored in a sealed desiccation chamber until imaging.

A Zeiss Auriga FIB/SEM was used to image and mill the samples. We did not sputter coat our unmilled samples with any conductive material because this can cover small features like those we are interested in seeing [BNA+13]. As a result, low accelerating voltage (0.9-1.2kV) and working distance (3-5mm) were used during imaging. Images were post processed with FIJI when needed [SACF+12]. For FIB milling a thick layer of Au/Pd was applied to the surface to reduce any effects from stray ions.

5.3 Results

A developmental study was done to determine the stage when nanostructures form on the cornea of the wild-type, OregonR, strain of *D. melanogaster*. A standardized staging timeline and nomenclature was adopted and used to reference developmental events [CR89],[BB81]. According to the standard, pupae were reared at 20°C and collected at 50, 60, 70, 80, 120, and 130 hours after the larvae stopped moving up the sidewall of the vial in which they were contained (indicating the beginning of

pupariation). SEM images of the pupae were taken at each time point to see if signs of the corneal nanostructures were visible. Images were also taken of adult flies to use as a reference (Figure 17). At earlier developmental stages exposing the cornea without damaging the eye becomes quite difficult. A thin membrane inside the pupa case covers the developing fly. This layer has a covering on the head, the operculum, which can be seen as a residue encasing the cornea where it could not be removed or washed away in some of the images. Significant developmental events occur in the retina at the time points chosen which were determined by work from previous groups. Their studies indicate that retinal/corneal development is most active between the P6 and P11 stages of development, or between 50 and 130 hours after pupariation when reared at 20°C [CR89],[BB81]. Before the P6 stage the head and body aren't formed enough to distinguish any kind of structure at all, and after the P11 stage the nanostructures are clearly visible on the developing eye.

During the P10 to P11 stages the lens is finished forming and the pseudocone is in the process of forming, this is also when the ocular bristles and dorsal chaetae start to darken. Images of the head and ommatidia at the P11 stage can be seen in Figure 18. The head and eyes appear to be fully developed and the corneal nanostructures are clearly present but still somewhat encased by the thin membrane that was covering the developing pupa. The membrane is fairly deteriorated at this stage though, leaving many large open patches where the corneal nanostructures can be seen. The bristles appear fully formed with only small amounts of debris on some of them.

In the P8 to P9 stages the eye turns from an amber to pink color and pigment granules have formed and can start to be found on the top of the retina. Figure 19 shows the development in the P9 stage after the eye turns pink in the pupa case.

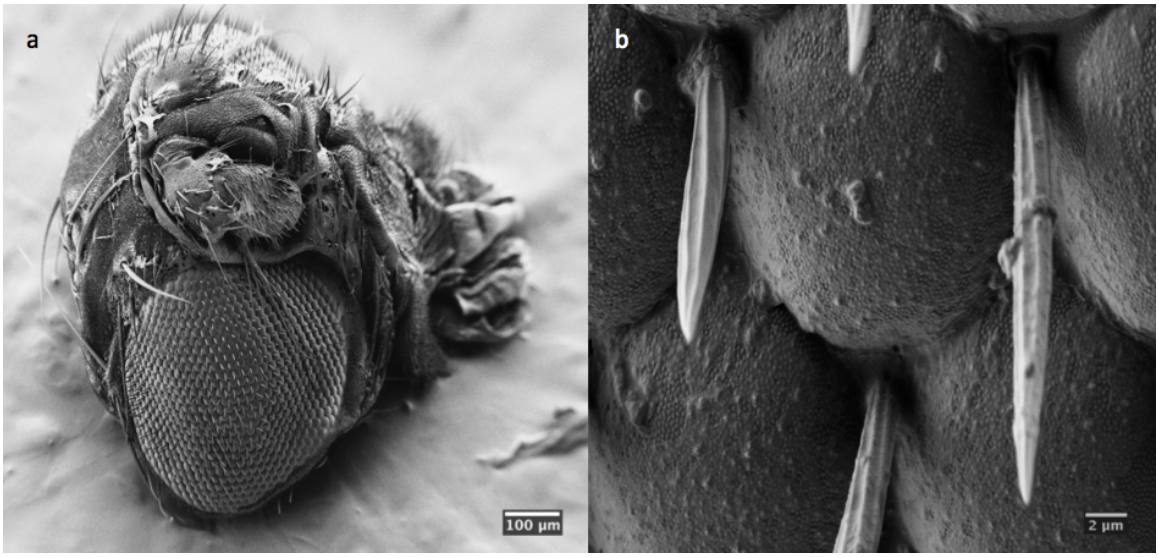

Figure 18. Head at P11 Stage of Development. a) Eyes and head look to be almost fully formed b) Ommatidia at P11 stage of development showing fully formed corneal nanostructures.

The head and eyes seem almost formed in Figure 19.b, but closer inspection of the ommatidia shows a film covering the ommatidia (Figure 19.b). Corneal nanostructures are visible beneath the membrane coating. At this stage the layer encasing the eye is thicker and is much less deteriorated than what is seen in Figure 18.b. The bristles in Figure 19.b show the encasing membrane layer must be strongly attached to the surface of the pupa throughout the development process as they do not remove the coating from the pupa. There are also clumps of stringy debris on top of the membrane coating which start to become visible in Figure 19.b.

Between the P7 and P8 stages, the developing eye turns a light peach color. This signifies the appearance of pigment granules at the base of the retina, the beginning of bristle formation, and later the release of the primary pigment cells form the bottom of the retina.

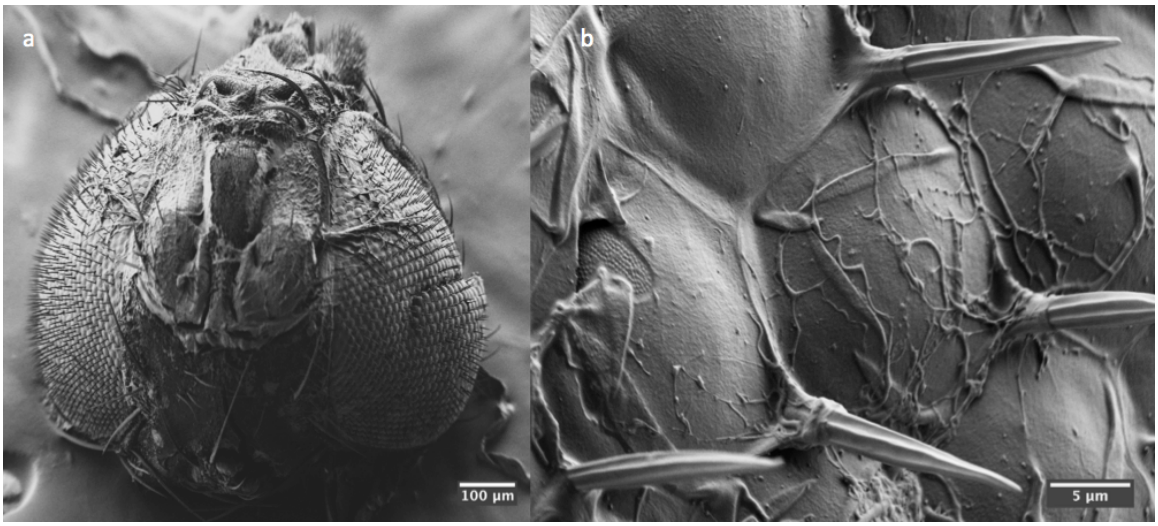

Figure 19. Head at P9 Stage of Development. a) Eyes seem almost fully formed. b) Ommatidia at P9 stage of development showing fully formed corneal nanostructures under a thick coating of membrane.

Both the release of the primary pigment cells and appearance of pigment granules could cause the formation of the corneal nanostructures, so images were taken at each time point to check for the corneal nanostructures (Figure 20). These events occur between 70 and 80 hours of pupal development (if reared at 20°C). Figure 20.a-c show a developing head at 80 hours when reared at 20°C. All of the previously mentioned developmental events have occurred. Figure 20.a shows a much less developed head with obvious remains of developmental debris, even after stringent washings. As seen before there is a membrane layer coating the surface of the pupal head, but unlike before the coating can be seen in the images even at low magnification although it does appear to be somewhat deteriorated along the eyes. When seen closer, there is a much thicker layer of the membrane coating with no signs of deterioration or gaps where the corneal nanostructures are exposed (Figure 20.b). There are also no fully formed bristles.

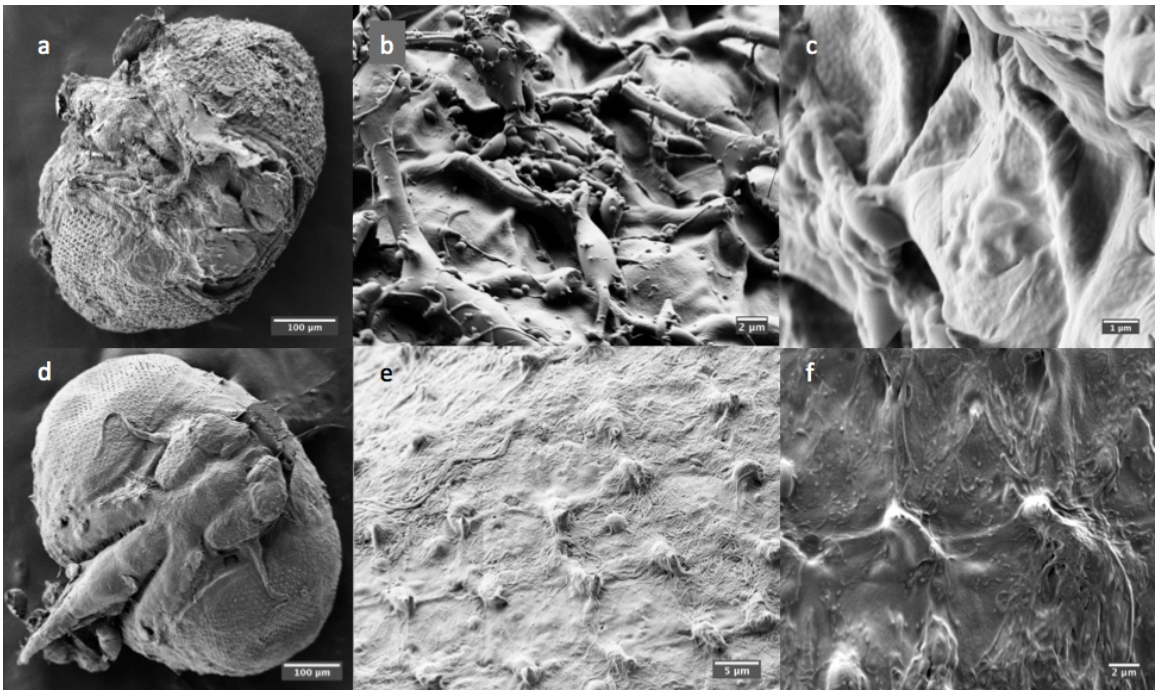

Figure 20. Developmental Images of Wild-type *D. melanogaster* Pupa. a) Head after 80 hours of development. b) Ommatidia after 80 hours of development. c) Closer image of corneal nanostructures at 80 hours development after pupariation. d) Head after 70 hours of development. e) Ommatidia after 70 hours development. f) Closer image of corneal nanostructures at 70 hours development. Corneal nanostructures can barely be recognized under a thick debris layer, but can be found in some areas.

At this stage of development the bristles are nothing more than malformed developmental debris on the corneal surface. Outlines of the corneal nanostructures are able to be distinguished on the developing ommatidia, blanketed beneath the membrane coating (Figure 20.c). This confirms the presence of these structures even at this early stage of development.

A pupa head at approximately 70 hours development is shown in Figure 20.d-f. This is when the eye first turns a light peach color, indicating the appearance of the pigment granules at the base of the retina.

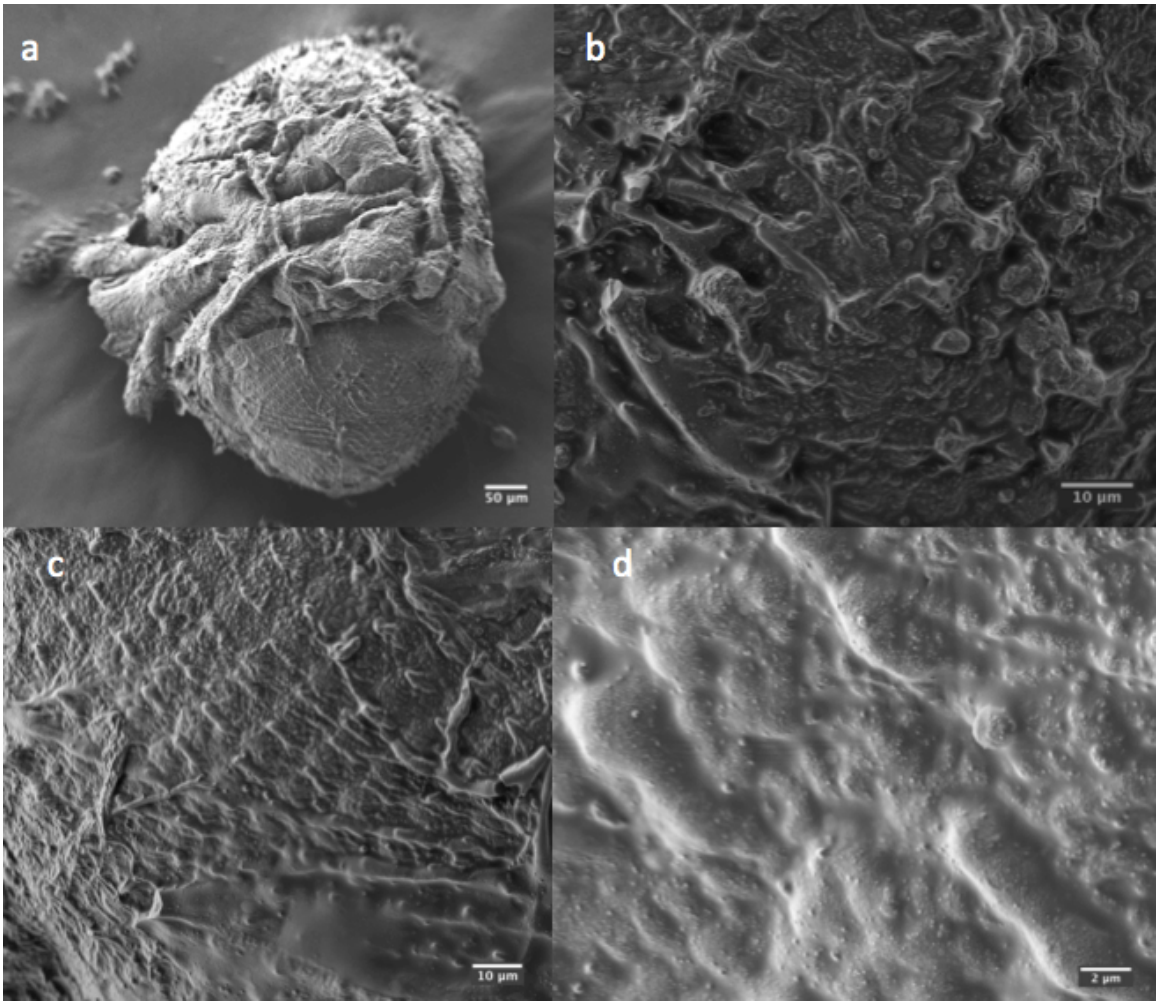

Figure 21. P7 Stage of Development. a) Head at P7 stage of development. b) Ommatidia at P7 stage of development showing secretions from possible bristle formation sites. c) Ommatidia at P7 stage of development showing a globular coating covering the surface. d) Globular coating covering the ommatidia surface.

This also signifies the development of the bristles and secretion of the lenses. The head in Figure 20.d is slightly less developed than at 80 hours and has a smooth and continuous coating covering its entirety that doesn't appear to have any deterioration at this stage.

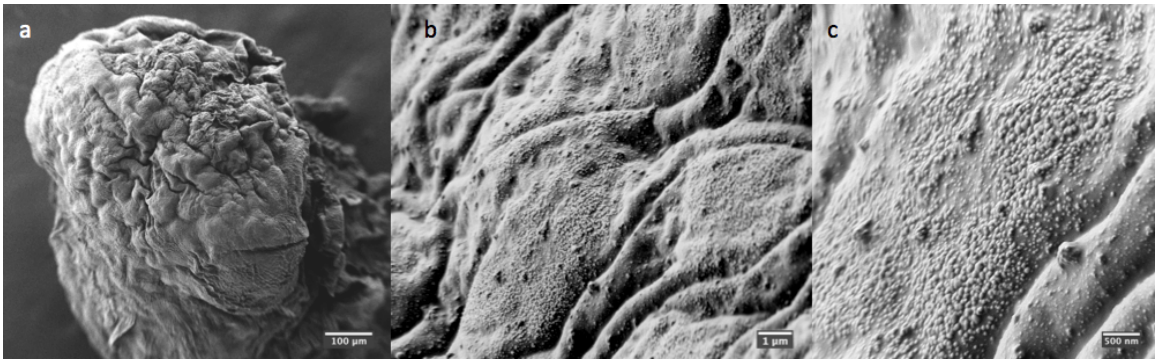

Figure 22. P6 Stage of Development. a) Head at P6 stage of development. b) Ommatidia at P6 stage of development. c) Small particles decorating the surface of the ommatidia at P6 stage of development.

Bristles appear as small knobs of stringy secretions covering the ommatidia in Figure 20.e. Signs of the corneal nanostructures are more difficult to find, but can be discovered under thinner layers of the membrane coating the ommatidia (Figure 20.f). Finding out when these structures appear will require going farther back in the development cycle.

The development of the fly body is not very far along at stages earlier than P8, which makes dissection for imaging more of a challenge. A successfully dissected specimen is shown in Figure 21. The head is somewhat developed with antennae and eyes distinguishable beneath a thick coating of debris (Figure 21.a). The debris seems much thicker and more rough than on the head seen at 70 hours development. Looking at the surface of the ommatidia reveals a much thicker coating than seen before (Figure 21.b). The sites where bristles will soon form appear somewhat raised and have a large amount of debris surrounding them, indicating that these sites may be responsible for secreting the coatings that cover the surface of the ommatidia in later developmental stages.

Figure 21.c shows an area of the ommatidia with less debris blocking the surface coating. Unlike in the later developmental stages the coating here is a globular mass of relatively large objects. Small nanoscopic particles are seen to be making up each of the larger globular masses when examined closer (Figure 21.d). These small particles do indeed appear to be the first signs of the developing corneal nanostructures. Interestingly, they seem to be dispersed across the cornea by a thick globular coating which may arise from the future sites of the developing bristles.

At the P6 stage the eyes and head are noticeably less developed as can be seen in Figure 22. Most features on the head have yet to begin development (Figure 22.a). Although the eyes can barely be recognized, patches of premature ommatidia can be found on the sides of the head (Figure 22.b). Here the globular coating and developmental debris secreted from the bristle sockets cannot be found. Instead there is a fairly continuous coating of the small particles which seemed to have made up the large masses of the globular coating formed in the next stage of development. Higher magnification of the coating shows the small particles are roughly the same size as the corneal nanostructures seen on a fully formed ommatidia, but they are more spherical than the corneal nanostrucutres seen on a fully formed adult ommatidia (Figure 22.c). The particles here also seem to have been being secreted, possibly from the future bristle sites, to decorate the entire surface of the ommatidia. These observations warrant further research of the internal structure to understand the mechanisms underlying the formation and assembly of the corneal nanostructure patterns found on adult fly eyes.

At any earlier stage of development the material inside the inner membrane of the pupa case is too premature to dissect anything more than cellular components.

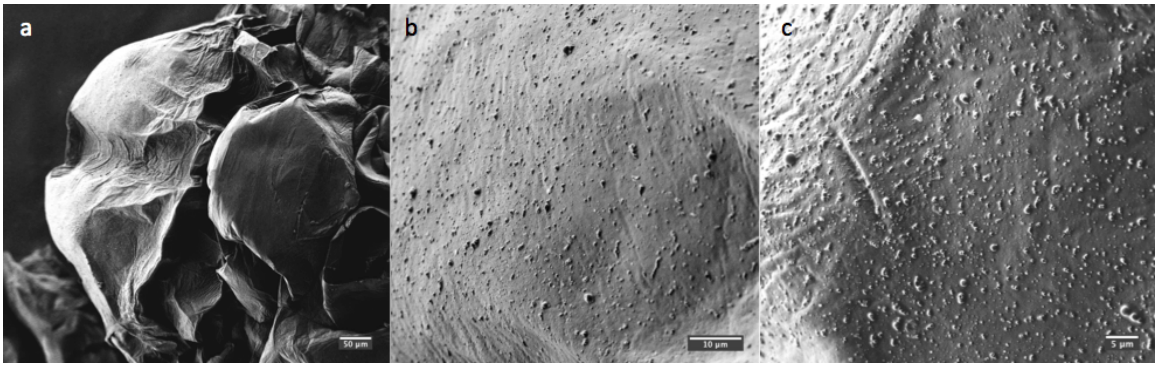

Figure 23. 49 Hour Pupa. a) Membrane covered head area of pupa at 49 hours. b) Exposed eye patch region. c) Sporadic globules decorating the surface of the eye patch region.

Figure 23 shows what could be prepared for imaging. The head is still forming, but translucent eye patches can be distinguished in a dissecting microscope. A small portion of the membrane was removed to expose the surface of the developing eye. Underneath the membrane the eye patch is shown to be sporadically covered in small globules (Figure 23.b). These globules are larger, and much less dense, than the particles seen decorating the surface of the ommatidia in Figure 22, indicating that they accumulate more before being incorporated with the globular coating. When seen closer the bigger globules are able to be found uniformly covering the entire eye region (Figure 23.c). It would seem these particles are being secreted from somewhere inside the eye and somehow spread across the surface in a uniform manner. Cross sectional images will be necessary to further investigate the developmental process.

Due to the lack of externally developed structure before the P6 stage of development, some 49 hour pupae (raised at 20°C) were prepared for focused ion beam (FIB) milling. A heavy sputter coating layer of AuPd was applied to help dissipate charging from exposed internal material that may not have been fixed well.

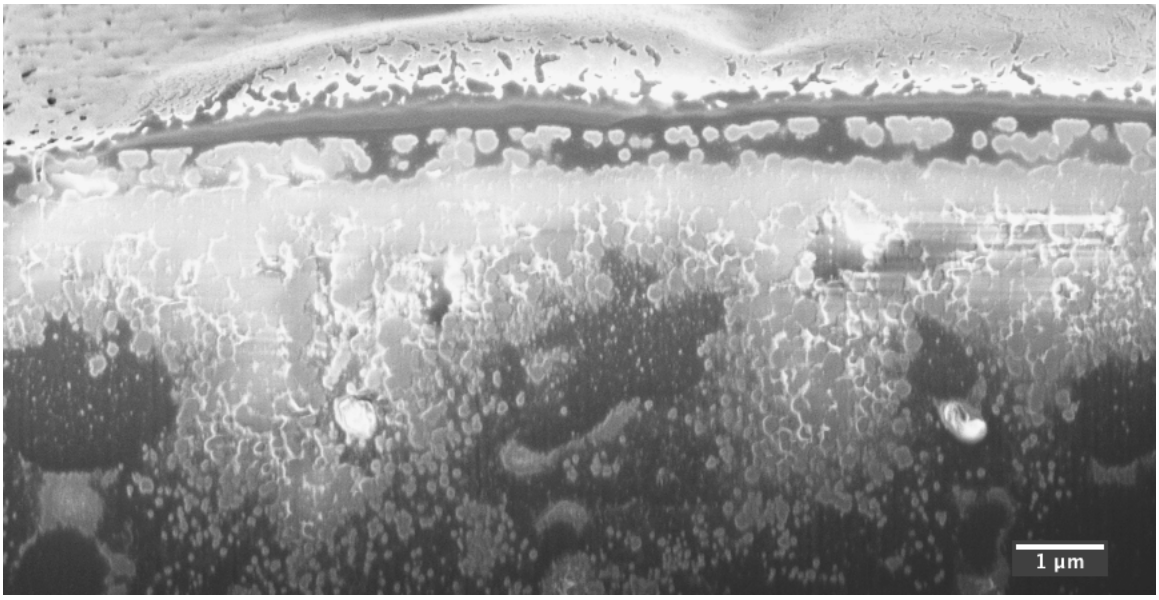

Figure 24. FIB/SEM Cross Sectional Image of Developing Pupa Eye After 49 Hours when Reared at 20°C.

This also protects the subsurface from damage caused by stray ions. The FIB/SEM was used to obtain a sequence of cross sectional images of the developing pupa. Images were taken after every slice done by the FIB (∼100nm) for a total of 365 images. Figure 24 shows one of the images. The image stack was then processed and rendered into a 3D volume using FIJI, enabling the visualization of a cross sectional image from any plane in the volume that was milled with a plug-in called Volume Viewer [SACF$^+$12]. The software was used along with the sequence of images taken with the FIB/SEM to get images from the XZ plane going through the eye. Figure 25 shows a selection of images going through the depth of the 49 hour developing fly eye.

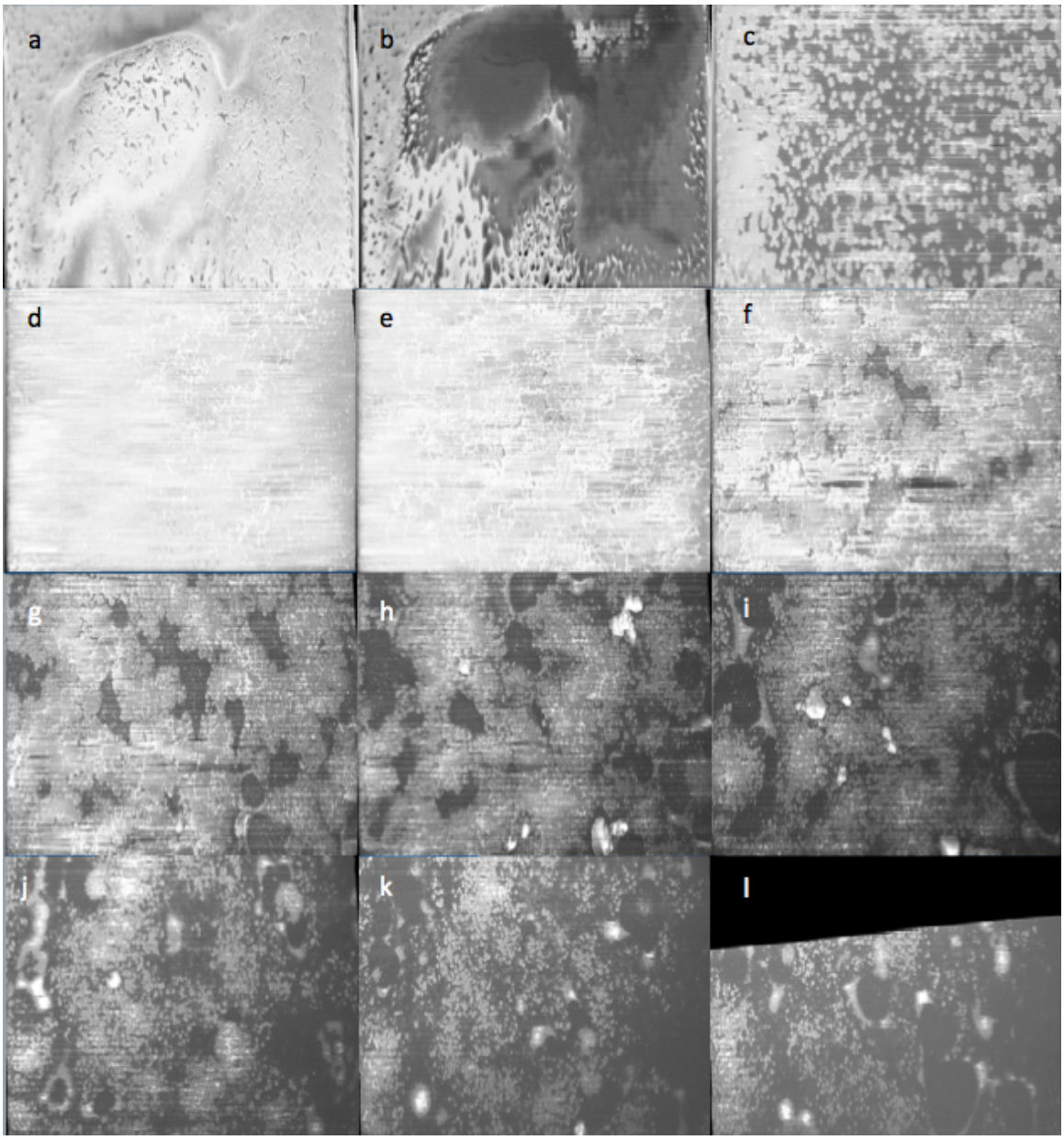

Figure 25. Sequence of Z-slices Reconstructed from FIB/SEM Milling of Pupa Eye After 49 Hours Development. a) Outer surface of the developing eye before milling. b) 300nm below surface. c) 700nm below surface. d) 1μm below surface. e) 1.5μm below surface. f) 2μm below surface. g) 2.5μm below surface. h) 3μm below surface. i) 3.5μm below surface. j) 4μm below surface. k) 4.5μm below surface. l) 5μm below surface.

It becomes clear, when comparing Figure 24 and Figure 25 together, that the globules seen decorating the eye of the 49 hour developing pupa are secreted uniformly from below the surface across the entire eye. Furthermore, the vesicles seem to form in clumps relatively deep below the surface of the eye (Figure 25.g-l) before begging conglomerated in to a thick, densely packed, layer just below the surface (Figure 25.d-f). Between the outer surface of the eye and the layer where the vesicles conglomerate, there is a thin section (∼800nm) where the vesicles are sent to the surface in a much less dense and uniform manner (Figure 25.c). The similarity in the distribution and size of the particles when comparing Figure 23.c and Figure 25.c are striking.

5.4 Discussion

A developmental study was performed in order to observe to formation of the corneal nanostructures on the eye of the fruit fly, *D. Melanogaster*. The structures were able to be located on the surface of the ommatidia up until the early stages of development (P6-P7). At approximately 50 hours after pupariation when reared at 20°C, the nanostructures seem to be pushing up from inside the surface of the lens as vesicular secretions (Figure 22). These secretions then accumulate and get incorporated into a globular mixture that coats the entire developing eye (Figure 21). This coating is then sandwiched between the developing eye and a thin membrane encasing the pupa (Figure 20). As the head grows larger and becomes more rigid inside, it seems the coating fuses with the membrane possibly creating a closed-packing effect to inhibit the hexagonal pattern to the small particles dispersed earlier (Figure 19). As the fly reaches full development the membrane shell deteriorates away leaving fully a formed array of corneal nanostructures. This is an interesting

method that could be used to decorate a surface with closed-packed nanopatterned structures.

Insight gained from this, and similar, research can help us in understanding nanostructure formation through the natural process of self-assembly. That knowledge could be used to make modern materials through novel processes.

CHAPTER VI

STUDYING STRUCTURAL BIOLOGY WITH FIB MILLING

6.1 Introduction

Focused ion beam milling combined with scanning electron microscopy (FIB/SEM) is commonly used for applications in the fields of material science, failure analysis, and device fabrication. The FIB can be precisely guided to mill intricate nanoscale features onto surfaces, or investigate subsurface defects at the nanoscale. There have been many breakthrough developments and technologies coming from its use in different ways. Another field the FIB/SEM is starting to have a great impact on is in the natural sciences. Observing and understanding how nature works has been key to the success of science from the very beginning. Now that we are able to investigate things at a scale smaller than ever before, it is wise to take a step back and look at things that we may think are fully understood again.

The power of the FIB when it comes to natural sciences is in the ability to perform accurate and precise serial sectioning and imaging at the nanometer scale. Figure 26.a shows a FIB image with an annotation indicating the area to be milled. Another image was taken after the milling to compare with the previous for accuracy (Figure 26.b). The milling was shown to be very accurate by successfully clearing material from only the areas outlined by the annotation. The FIB was is set to mill the area slice by slice starting from the face end opposite the red face and ending with the red face. The final cut (indicated by the red face) leaves a clean cross-sectional image when using a finely tuned beam.

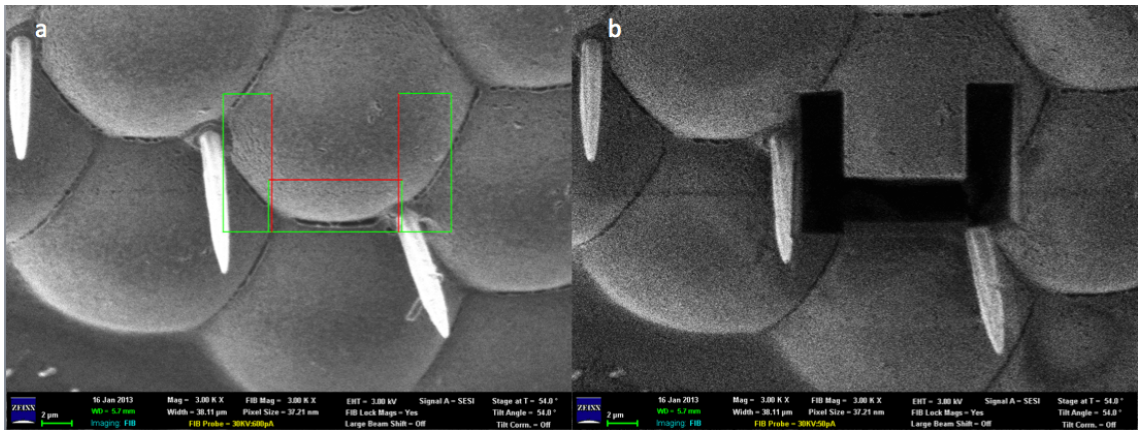

Figure 26. FIB Images of *D. Melaonogaster* Eye. a) Before milling with annotation showing pattern to be milled. b) After milling of the pattern is completed.

This process cane used to generate slices of a sample with single-digit nanometer thickness. TEM lamella preparations also greatly benefitted by FIB/SEM milling. Lamella can be milled from surfaces at exact locations and thinned until features of interest become visible. This level of precision and accuracy is unprecedented in an unltramicrotome system for getting TEM lamella.

There are a number of parameters to adjust when doing FIB/SEM milling in order to get quality, usable, data. Many of these parameters are the same as those found in typical SEM imaging like focus, stigmatic, aperture alignment, and beam strength. This means that similar adjustments need to be made for each system, but separately. Once beam characteristics are optimized for both systems, they need to be brought into a coincidence point. This enable both beams to be hitting the same spot on a sample and is done by raising the stage to a certain working distance where the two cross (5mm for the Auriga used here). Fine height adjustments of the stage are then made while imaging to get the beams in exact coincidence.

After the coincidence point is found, it is necessary to make more adjustments if a new location of the sample is moved to.

Once coincidence is found between the FIB and SEM, it is necessary to align and optimize the FIB for each milling probe that is planned to be used. This is done by finding, or milling, a feature to use as an alignment mark. The probes are all adjusted similar to how the SEM, including focus, stigmatic, and aperture alignment as well as being calibrated to be centered at the same location. This way all the probes are well shaped and looking at the same spot. This is a very important step in getting quality data. Figure 27 shows an example of an artifact called curtaining. Curtaining occurs when the FIB is not in focus or not milling deep enough. The dark area in the bottom half of Figure 27.a has a wavy line at the top which is lower in Figure 27.b and near the bottom of the image in Figure 27.c. When multiple frames are seen in series, it appears as a waviness in the image resembling flowing curtains. This causes distortions in the images which effect the quality of data that can be made through post processing.

Sample preparation for FIB/SEM milling is another crucial step in order to obtain quality imaging results. Bombardment of the surface with the more massive ions used by the FIB can cause more damage than is seen with a typical electron beam. It is often possible to see a clear outline an area that was being imaged after the magnification is reduced. To avoid artifacts associated with these issues in imaging, it is necessary to coat the surface that is going to be milled with a thick coating to block any surface or stray ion damage. The thick coating over the surface also enables the details of the surface to be obtained that would normally be damaged by slicing in an ultramicrotome.

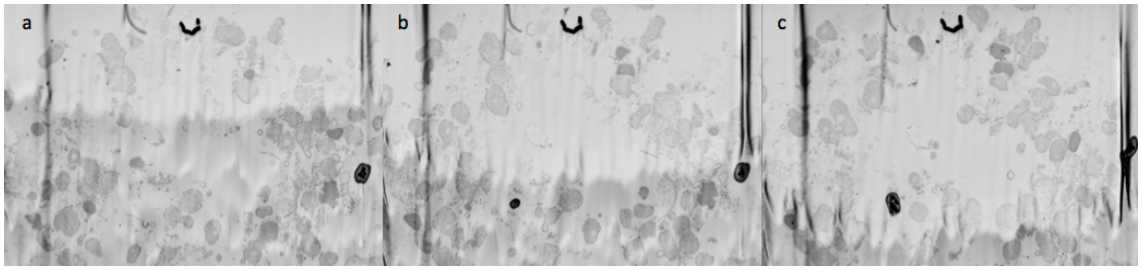

Figure 27. Example of Curtaining and Stray Ion Damage.

If the coating is too thin, stray ions can break through and cause ion implantation in the sample. This results in streaks and holes in the data gathered (Figure 27). The streak going through the image shown on the right side of Figure 27.a and progressing through the sample as slices are taken (Figure 27.b,c) is an example of ion implantation due to too thin of a surface coating.

The FIB/SEM system offers many benefits to the natural sciences, and should be used more often as an investigational tool. Using a gallium beam, we are already able to precisely mark an area of interest and cut out a TEM lamella with a thickness below 5nm. With the introduction of other ion sources than gallium, including neon and helium, the possibility for even more groundbreaking research is surely on the horizon. More powerful than the milling of lamella for TEM is the ability to serially section an area while taking SEM images after each slice. This technique allows for the digital reconstruction of the entire volume that has been milled/imaged using advanced imaging processing software.

6.2 Materials & Methods

The *S. cerevisiae* strains used in this study was W303-1A (ATCC stock number, 208352) Frozen stocks were maintained at -80°C. For each experiment, colonies from

freshly streaked YPD plates were used. Liquid YPD (Yeast extract, Peptone, Dextrose, Water) media was inoculated with one colony per 5ml. Liquid cultures were grown overnight with shaking ∼200rpm at 20°C to an OD600 ∼1.5 at which point fresh cultures were spiked to an OD600 ∼0.2 and incubated with shaking for 3-5 hours at 30°C to an OD600 ∼(0.4-0.6) indicative of mid-log phase growth. OD600 measurements were made using a Thermo Scientific NANODROP 2000C spectrophotometer and viability counts $\sim 10^7$ cells/mL were made using serial dilution plating.

The following strains of *D. melanogaster* were used in these experiments: Oregon-R strain was used as the wild-type control (*Bloomington Stock Center # 113*); *white eyed/w1118* (*Bloomington Stock Center #5905*) *roughoid/ru* (*Bloomington Stock Center #575*).

Adult *Drosophila* flies were reared at 20°C and on a standard cornmeal/molasses medium. Adult flies were collected for sample preparation three days after eclosure and euthanized by cold exposure, -20°C for ∼1 hour. The samples were fixed in a solution consisting of 2.5% gluteraldehyde (Ted Pella 18426) and 2% formaldehyde (Ted Pella 18505) in a 0.1M cacodylate buffer (pH 7.4) for ∼12h. Fixation ensured that the cuticle did not collapse during desiccation, presumably by crosslinking the underlying soft tissue. After fixation samples were washed three times in distilled water and dehydrated in an acetonitrile series (50%, 70%, 90%, 95% and 100% twice). Once fixed and dehydrated, the specimens were mounted on EM mounting stubs (Ted Pella 16111) and were secured to the stub with double sided carbon tape or silver paste. Some samples were embedded in spurs resin for processing with the FIB. This consisted of mixing the dehydrated samples in a series of 25%, 50%, 70%, 90%, 95%, 100% twice acetonitrile:spurs resin mixtures, for 30 minutes each at 70°C (except the

last step which was done for 8 hours). Before curing for 8 hours most of the resin encasing the sample was attempted to be removed by slowly dragging the sample across aluminum foil until only a minimal amount remained coating the surface. Failure to remove the surface resin coating can result in the inability to recognize features on the sample surface, as well as increase the amount of time needed to perform the milling tasks. Prepared specimens were stored in a sealed desiccation chamber until imaging.

Samples are sputter coated with a thick (∼60nm or more) layer of Au (Pelco model 3 Sputter Coater 91000). Once available, other samples were sputtered with AuPd using a Leica EM ACE200 equipped with a quartz crystal microbalance to monitor layer thickness, and an angled, rotating, stage with planetary motion to ensure an even coating. Carbon coating was also performed on the Leica EM ACE200 using a flat stage without rotation.

Soft tissue from larvae and pupae were dissected in a phosphate saline buffer solution, fixed in a solution consisting of 2.5% gluteraldehyde and 2% formaldehyde for 12 hours at 4°C. Careful dissection before fixation as necessary to avoid damaging the developing soft tissue. Samples were dehydrated immediately in the acetonitrile series and then dried and mounted onto the SEM stub.

A Zeiss Auriga FIB/SEM, (Carl Zeiss, Oberkochen, Germany) was used to characterize and mill samples. The working distance for FIB/SEM imaging/milling is close to 5mm in order to maintain a point of coincidence between the two beams. Accelerating voltage was 1-5kV for the SEM and 30kV for the FIB. The FIB accelerating voltage is regulated to maintain an emission current of 2μA. Apertures are used to select different probes for milling with the FIB.

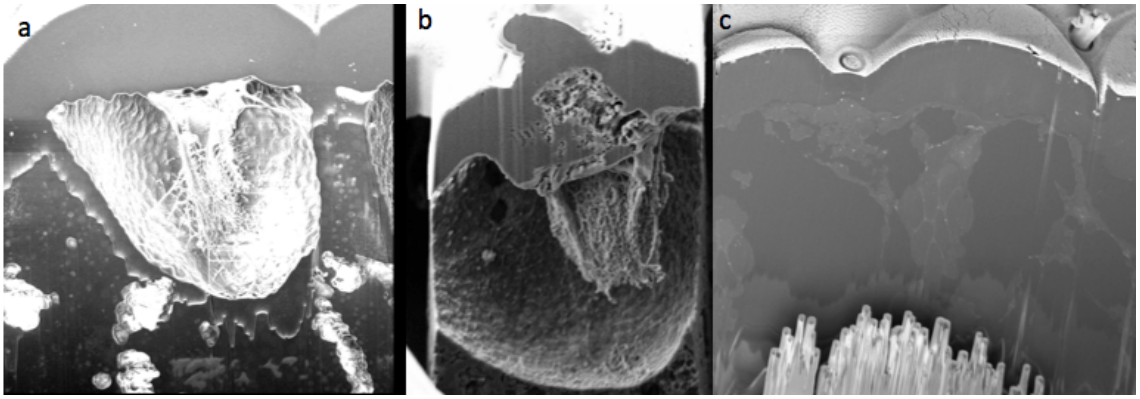

Figure 28. SEM Images of Fruit Fly Ommatidia Milled with the FIB. a) Wild type Oregon-R strain used as a control. b) *Roughoid/ru* mutant. c) *White-eyed/w1118* mutant.

These probes can have currents ranging from 1pA-40nA depending on the application. Typically 50pA is suitable for basic imaging without excessive sample damage. The accelerating voltage on the can be reduced to do work requiring minimal sample damage, like TEM lamella thinning.

Image processing was performed using the open source variant of ImageJ called FIJI [SACF$^+$12]. This software was used to adjust image attributes like brightness and contrast as well as performing 3D rendering of data gathered from the FIB/SEM.

6.3 Results

Observations of the natural world created the very foundations of science. Using FIB/SEM technology now allows scientists to make observations that could never have been made before. This can impact the fields of material science, chemistry, biology, and metrology just to name a few. One way the FIB/SEM can achieve this is by milling away large areas of material to reveal detailed cross-sections in samples. An advantage of using a FIB/SEM over a typically used system like a TEM is that

there is no need to prepare thin sectioned lamella prior to imaging. The FIB makes slices that can be much thinner that a typical TEM lamella, giving it the ability to accurately specify a region of interest on a specimen and proceed with the milling and imaging without the need for extra equipment. Figure 28 shows a milled area exposing cross-sections of ommatidia in the eyes of the fruit fly. The sample shown in Figure 28.a is of the wild-type Oregon-R strain and is used to represent a normally developed adult fruit fly eye. Figure 28.b shows a fly with a well characterized eye mutation causing a malformed ommatidia, *roughoid/ru*. Here detailed structural information about the exact location of interest in the malformed cell can be characterized, which can be difficult for slices prepared conventionally for TEM. Figure 28.c shows a fly with an eye mutation causing the pigment granules not to form. This makes the typical red eyed fly have an opaque while eye. The small circles shown in the pigment cells around the pseudocone in Figure 28.a indicating pigment granules cannot be found in Figure 28.c. Findings from observations like these can add knowledge about the systems and mechanisms of things that may have previously been thought to have been fully understood.

Rather than selecting just a single area to mill and getting one cross-sectional image, if desired an SEM image can be taken after a predetermined number of slices are mede by the FIB. As the slice thickness can be very small in some cases (less than 5nm) a great deal of data can be generated about a sample. Figure 29 shows a selection of SEM images of serial slices taken of a yeast cell on a nanostructured surface. As the FIB slicing progresses, material is removed exposing fresh layers to image from the front to back of the cell.

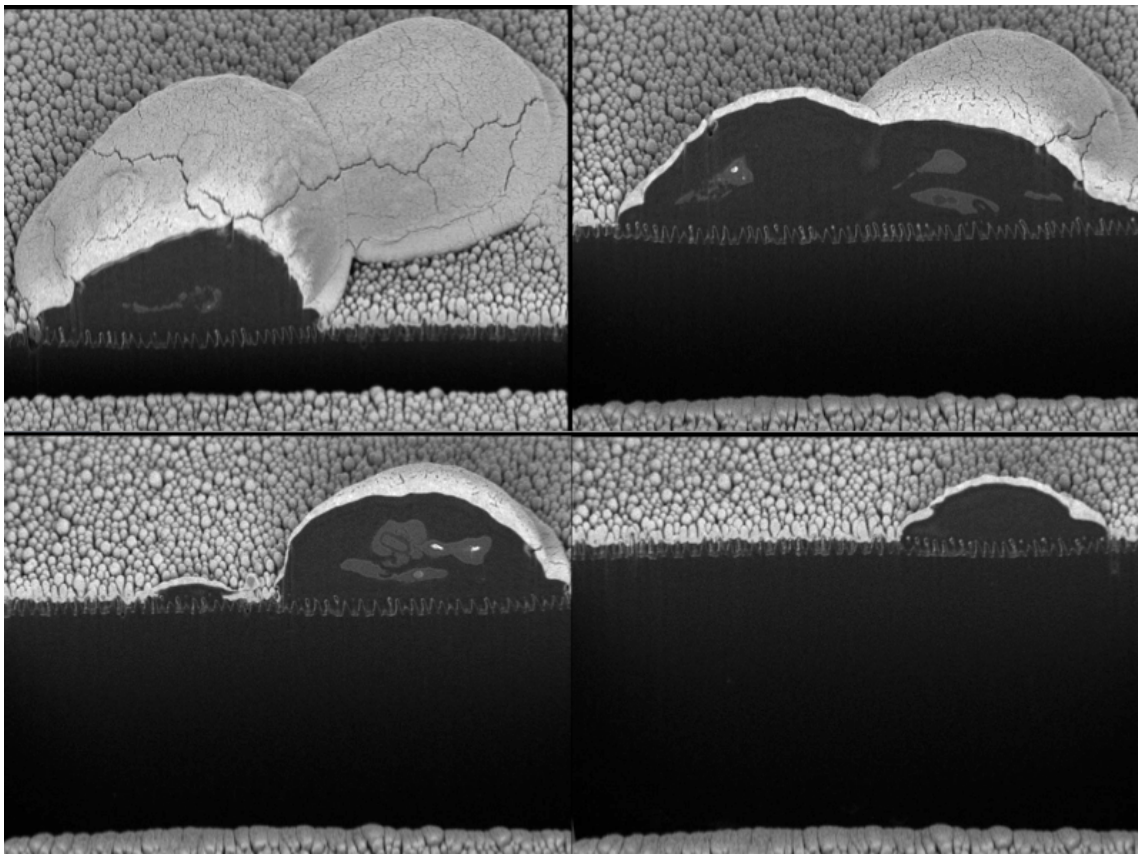

Figure 29. Serial SEM Images of Yeast Cells Being Milled with the FIB.

Accurate reconstructions of any view in the yeast cell can be created using the image sequence data from the milling. Figure 30 has a line indicating the location of a reconstructed z-slice of the cell and the nanostructured surface it is on. Figure 30.c shows the cell/substrate interface in a way that could not otherwise be seen. This has many advantages over the technique of serial slicing using an ultramicrotome, the main one being that the slicing/imaging does not need to be along the plane you wish to get information about.

Staining biological specimens in order to view cellular components under a microscope has been standard practice since its invention.

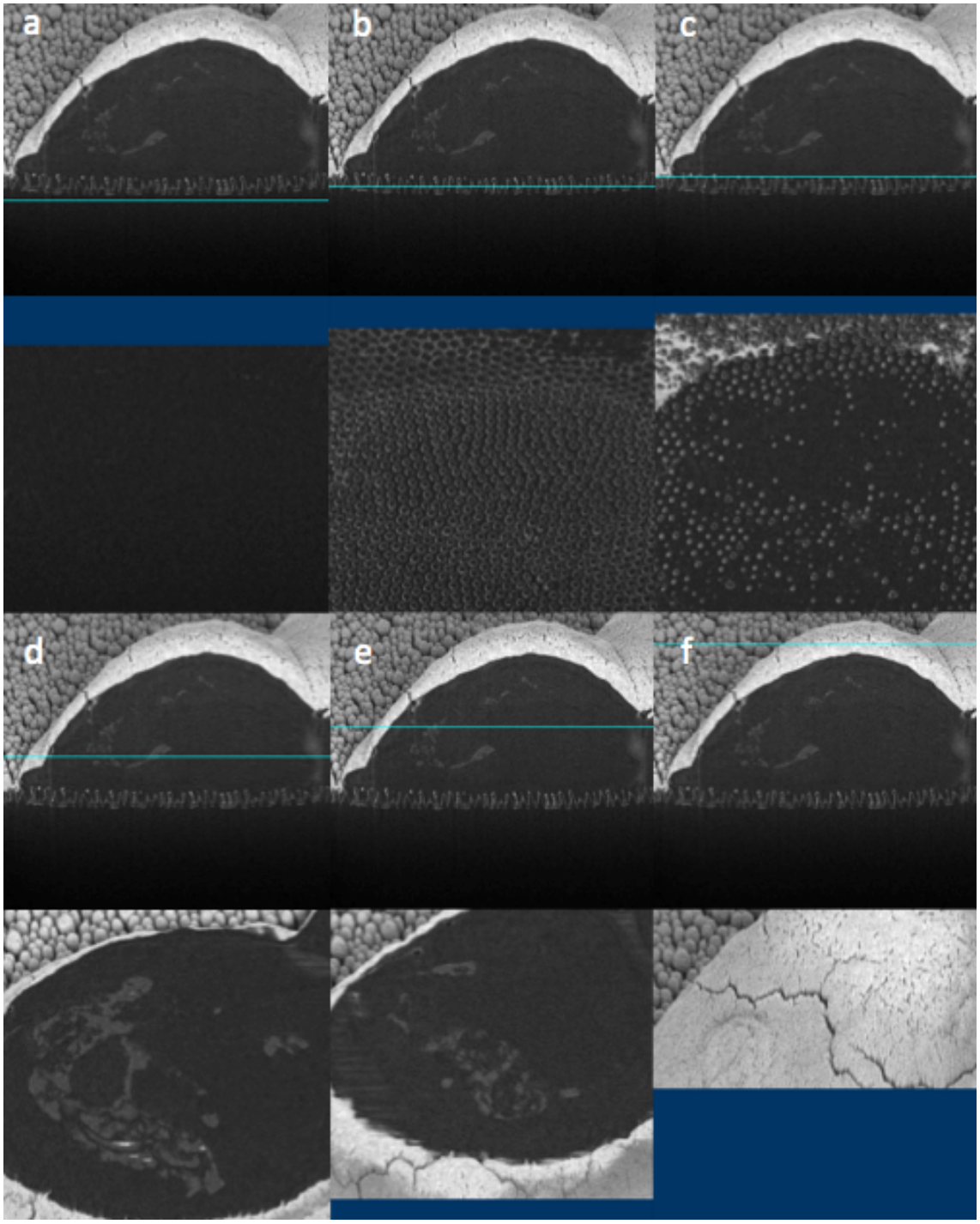

Figure 30. SEM Images with Corresponding Reconstructed Z-slices. a) Below the substrate the cells have settled on. b) At the bottom of the interface of the substrate and yeast cell. c) At the top of the interface of the substrate and yeast cell. d) Base of the yeast cell. e) Half-way through the yeast cell. f) Top of the yeast cell.

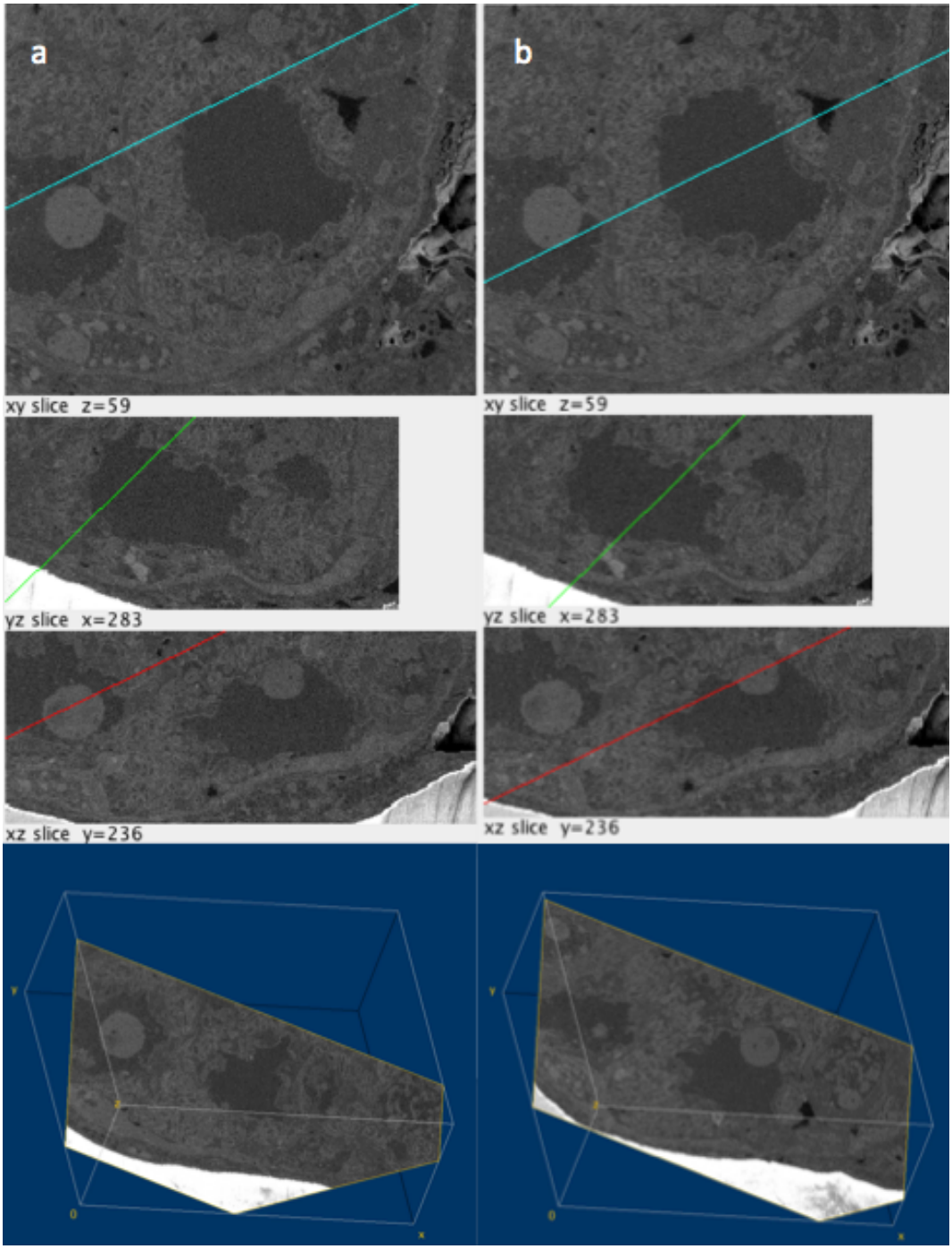

Figure 31. Series of Volumetric Slices of a Stained Specimen. a) First slice taken from within the surface of the specimen going through a nucleus. b) Second slice taken going through another nucleus.

TEM and SEM systems use staining with heavy metal ions to enhance electron density in certain areas of the cell. Some cellular components can have natural electron dense areas, as seen in the yeast cell from Figure 30.d and e. Those specimens were not stained before milling, but still some components of the cell were visible. An example of a stained specimen can be seen in Figure 31. Unlike typical bright-field TEM images where staining increases the atomic weight of cellular components, essentially blocking electrons from the electron beam from penetration, are usually visualized as dark objects on a bright background. In the SEM, the same staining effects cause the cellular components to have increased electron density, thus providing more contrast, resulting in bright objects on a dark background (Figure 31). In order to see the information in a more traditional fashion, it is possible to process the received data to create the bright-field look. Inverting the colors in the images and adjusting the brightness/contrast levels changes bright objects on a dark background into dark objects on a bright background. Staining allows many cellular components to be distinguished and analyzed at the nanometer scale, Figure 31.a and b show views from the Volume Viewer plug-in made for FIJI [SACF$^+$12]. The XY plane is shown at the top and is the data gathered from the SEM image sequence. Below the XY plane view are the YZ and XZ plane views that are rendered by the software. When the slices taken from the FIB closely match the pixel size of the images taken by the SEM, images of the same quality can be visualized at any point and from any plane from the volume of the are milled. This is demonstrated below the sectional plane images. Outlines of a 3D prism represent the volume milled by the FIB in which sections can be visualized. Inside each prism is a slice taken at an obscure angle corresponding to the slice locations in the images above.

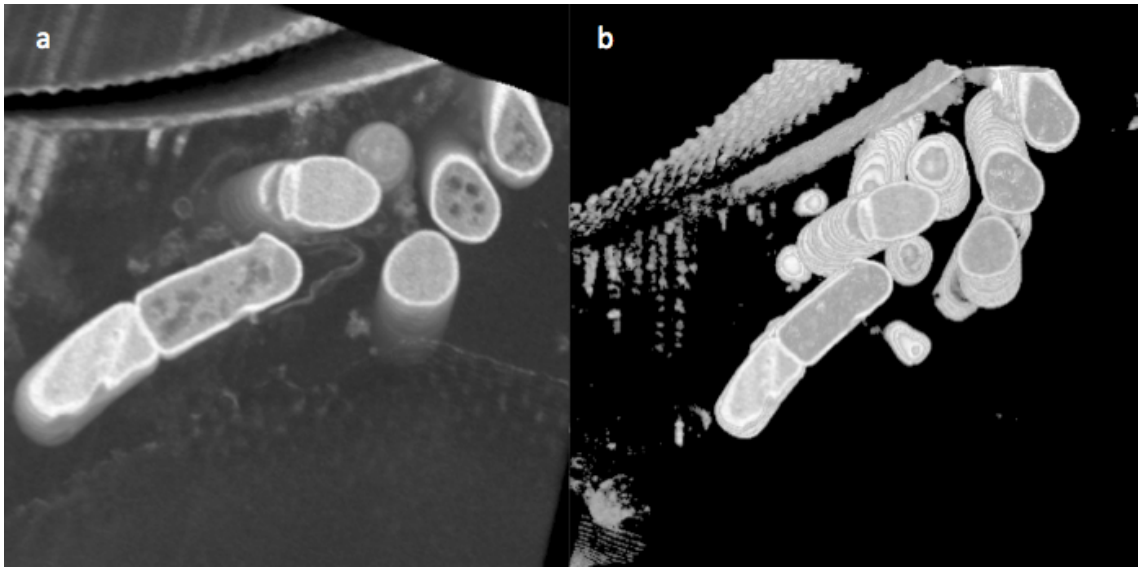

Figure 32. 3D Rendering from FIB/SEM Data. a) Rendering with no adjustments made. b) Rendering with color threshold attribute increased.

Several cellular components can be distinguished, as well as their interaction and connections to surrounding organelles.

It can be somewhat difficult for some to visualize the orientation and spatial locations of objects in three dimensions when only given two dimensional data, especially when only using the imagination. Figure 32 shows a 3D rendering from FIB/SEM data made using FIJI. Image stack registration is required to align all the images in three dimensions. When visualized in the 3D viewer it is much easier to determine locations and orientations of different objects (Figure 32.a), especially after adjusting image parameters, like the color threshold value, to optimize visualization (Figure 32.b).

6.4 Discussion

Microscopy has provided groundbreaking revelations in science from its very existence. Now we have the ability to see things at a smaller scale than ever before. With the ability to see detailed imaged of nanoscale features, the use of TEM has offered advantages many different fields of science. The issue with TEM is there typically is just one or a few slices that can be registered to try and get an idea of what is going on throughout a larger object. At times, this can be very difficult to interpret and may introduce some flaws in analysis for that reason. With increasing levels of resolution available using the FIB/SEM, it is quickly coming close to matching the level of detail that can be seen with the TEM and is certainly already at a high enough level to perform many quality experiments.

Unlike TEM, the FIB/SEM gathers data from the entire volume that is milled through. With slice thickness becoming smaller than 5nm as technology increases, over 200 images per micrometer can be collected from a sample at as high of resolution as the SEM can achieve. Observations of objects at this level of detailed can give great insight into current topics that are though of as mysteries in nature, which could lead to the development of many new device designs and applications.

REFERENCES

[ACP94] P N Adler, J Charlton, and W J Park, *The drosophila tissue polarity gene inturned functions prior to wing hair morphogenesis in the regulation of hair polarity and number.*, Genetics **137** (1994), no. 3, 829–36.

[AGLD10] David Alsteens, Melissa C. Garcia, Peter N. Lipke, and Yves F. Dufrêne, *Force-induced formation and propagation of adhesion nanodomains in living fungal cells*, Proceedings of the National Academy of Sciences **107** (2010), no. 48, 20744–20749.

[AKvVM12] Paul F. A. Alkemade, Emma M. Koster, Emile van Veldhoven, and Diederik J. Maas, *Imaging and nanofabrication with the helium ion microscope of the van leeuwenhoek laboratory in delft*, Scanning **34** (2012), no. 2, 90–100.

[ALH+00] Kellar Autumn, Yiching A Liang, S Tonia Hsieh, Wolfgang Zesch, Wai Pang Chan, Thomas W Kenny, Ronald Fearing, and Robert J Full, *Adhesive force of a single gecko foot-hair*, Nature **405** (2000), no. 6787, 681–685.

[ASB+09] Marco Arnold, Marco Schwieder, Jacques Blummel, Elisabetta A. Cavalcanti-Adam, Monica Lopez-Garcia, Horst Kessler, Benjamin Geiger, and Joachim P. Spatz, *Cell interactions with hierarchically structured nano-patterned adhesive surfaces*, Soft Matter **5** (2009), 72–77.

[ASL+02] Kellar Autumn, Metin Sitti, Yiching A Liang, Anne M Peattie, Wendy R Hansen, Simon Sponberg, Thomas W Kenny, Ronald Fearing, Jacob N Israelachvili, and Robert J Full, *Evidence for van der waals adhesion in gecko setae*, Proceedings of the National Academy of Sciences **99** (2002), no. 19, 12252–12256.

[BARB12] Stuart A. Boden, Asa Asadollahbaik, Harvey N. Rutt, and Darren M. Bagnall, *Helium ion microscopy of lepidoptera scales*, Scanning **34** (2012), no. 2, 107–120.

[BB81] S. Paul Bainbridge and Mary Bownes, *Staging the metamorphosis of drosophila melanogaster*, Journal of Embryology and Experimental Morphology **66** (1981), no. 1, 57–80.

[BBK93] D. F. Bray, J. Bagu, and P. Koegler, *Comparison of hexamethyldisilazane (hmds), peldri ii, and critical-point drying methods for scanning electron microscopy of biological specimens*, Microscopy Research and Technique **26** (1993), no. 6, 489–495.

[BCK+12] Michael D Bartlett, Andrew B Croll, Daniel R King, Beth M Paret, Duncan J Irschick, and Alfred J Crosby, *Looking beyond fibrillar features to scale gecko-like adhesion*, Advanced Materials **24** (2012), no. 8, 1078–1083.

[BF09] James Bullock and Walter Federle, *Why have more than one pad per leg? determining the mechanical and adhesive properties of hairy attachment pads in beetles*, Comparative Biochemistry and Physiology Part A: Molecular & Integrative Physiology **153** (2009), no. 2, S130.

[BF11] James MR Bullock and Walter Federle, *Beetle adhesive hairs differ in stiffness and stickiness: in vivo adhesion measurements on individual setae*, Naturwissenschaften **98** (2011), no. 5, 381–387.

[BG01] RG Beutel and SN Gorb, *Ultrastructure of attachment specializations of hexapods (arthropoda): evolutionary patterns inferred from a revised ordinal phylogeny*, Journal of Zoological Systematics and Evolutionary Research **39** (2001), no. 4, 177–207.

[BG06] Rolf G Beutel and Stanislav N Gorb, *A revised interpretation of the evolution of attachment structures in hexapoda with special emphasis on mantophasmatodea*, Arthropod Systematics & Phylogeny **64** (2006), no. 1, 3–25.

[BGM68] C. G. Bernhard, G. Gemne, and A. R. Moller, *Modification of specular reflexion and light transmission by biological surface structures*, Quarterly Reviews of Biophysics **1** (1968), 89–105.

[BGS70] C.G. Bernhard, G. Gemne, and J. Sällström, *Comparative ultrastructure of corneal surface topography in insects with aspects on phylogenesis and function*, Zeitschrift für vergleichende Physiologie **67** (1970), no. 1, 1–25 (English).

[BJ96] Alan Boyde and Sheila J Jones, *Scanning electron microscopy of bone: instrument, specimen, and issues*, Microscopy research and technique **33** (1996), no. 2, 92–120.

[BM62] C. G. Bernhard and William H. Miller, *A corneal nipple pattern in insect compound eyes*, Acta Physiologica Scandinavica **56** (1962), no. 3-4, 385–386.

[BMM63] C. G. Bernhard, William H. Miller, and Aage R. Moller, *Function of the corneal nipples in the compound eyes of insects*, Acta Physiologica Scandinavica **58** (1963), no. 4, 381–382.

[BNA+13] Adam Boseman, Kyle Nowlin, Sarmadia Ashraf, Jijin Yang, and Dennis LaJeunesse, *Ultrastructural analysis of wild type and mutant drosophila melanogaster using helium ion microscopy*, Micron **51** (2013), no. 0, 26 – 35.

[Bra07] Silvia E Braslavsky, *Glossary of terms used in photochemistry, (iupac recommendations 2006)*, Pure and Applied Chemistry **79** (2007), no. 3, 293–465.

[Car07] Richard W Carthew, *Pattern formation in the drosophila eye*, Current opinion in genetics & development **17** (2007), no. 4, 309–313.

[CBBF10] Christofer J Clemente, James MR Bullock, Andrew Beale, and Walter Federle, *Evidence for self-cleaning in fluid-based smooth and hairy adhesive systems of insects*, The Journal of experimental biology **213** (2010), no. 4, 635–642.

[CCVB95] Y Chen, VE Centonze, A Verkhovsky, and GG Borisy, *Imaging of cytoskeletal elements by low-temperature high-resolution scanning electron microscopy*, Journal of microscopy **179** (1995), no. 1, 67–76.

[CKMC94] Kelly Cant, Brenda A Knowles, Mark S Mooseker, and Lynn Cooley, *Drosophila singed, a fascin homolog, is required for actin bundle formation during oogenesis and bristle extension.*, The Journal of cell biology **125** (1994), no. 2, 369–380.

[CR89] Ross L. Cagan and Donald F. Ready, *The emergence of order in the drosophila pupal retina*, Developmental Biology **136** (1989), no. 2, 346 – 362.

[CR09] Douglas E Chandler and Robert W Roberson, *Bioimagingcurrent concepts in light and electron microscopy*, Jones and Bartlett Publishers, Sudbury, Mass., 2009.

[DCF10] Jan-Henning Dirks, Christofer J Clemente, and Walter Federle, *Insect tricks: two-phasic foot pad secretion prevents slipping*, Journal of The Royal Society Interface **7** (2010), no. 45, 587–593.

[DF11] Jan-Henning Dirks and Walter Federle, *Mechanisms of fluid production in smooth adhesive pads of insects*, Journal of The Royal Society Interface (2011), rsif20100575.

[DGMRSR12] Andrea Di Giulio, Emanuela Maurizi, Marco Valerio Rossi Stacconi, and Roberto Romani, *Functional structure of antennal sensilla in the myrmecophilous beetle paussus favieri (coleoptera, carabidae, paussini)*, Micron **43** (2012), no. 6, 705–719.

[DKSM+11] Petra Ditsche-Kuru, Erik S Schneider, Jan-Erik Melskotte, Martin Brede, Alfred Leder, and Wilhelm Barthlott, *Superhydrophobic surfaces of the water bug notonecta glauca: a model for friction reduction and air retention*, Beilstein journal of nanotechnology **2** (2011), no. 1, 137–144.

[FCFZ12] Daniel Fox, Yanhui Chen, Colm C Faulkner, and Hongzhou Zhang, *Nano-structuring, surface and bulk modification with a focused helium ion beam*, Beilstein journal of nanotechnology **3** (2012), no. 1, 579–585.

[Fed06] Walter Federle, *Why are so many adhesive pads hairy?*, Journal of Experimental Biology **209** (2006), no. 14, 2611–2621.

[FHA02] Xiaoyin Fei, Biao He, and Paul N. Adler, *The growth of drosophila bristles and laterals is not restricted to the tip or base*, Journal of Cell Science **115** (2002), no. 19, 3797–3806.

[FRCF02] Walter Federle, Mathis Riehle, Adam SG Curtis, and Robert J Full, *An integrative study of insect adhesion: mechanics and wet adhesion of pretarsal pads in ants*, Integrative and Comparative Biology **42** (2002), no. 6, 1100–1106.

[GCR+03] Gregory M Guild, Patricia S Connelly, Linda Ruggiero, Kelly A Vranich, and Lewis G Tilney, *Long continuous actin bundles in drosophila bristles are constructed by overlapping short filaments*, The Journal of cell biology **162** (2003), no. 6, 1069–1077.

[Gem66] G Gemne, *Ultrastructural ontogenesis of cornea and corneal nipples in the compound eye of insects*, Acta Physiologica Scandinavica **66** (1966), no. 4, 511–512.

[GG92] Payel Georgiev and Tatiana Gerasimova, *Genes involved in the development of bristles and hairs in drosophila melanogaster*, Genetica **87** (1992), no. 1, 31–35.

[Gor98] Stanislav N Gorb, *The design of the fly adhesive pad: distal tenent setae are adapted to the delivery of an adhesive secretion*, Proceedings of the Royal Society of London. Series B: Biological Sciences **265** (1998), no. 1398, 747–752.

[GSG+12] Ce Guo, JiuRong Sun, YingBin Ge, WenBo Wang, DaPeng Wang, and ZhenDong Dai, *Biomechanism of adhesion in gecko setae*, Science China Life Sciences **55** (2012), no. 2, 181–187.

[GSP+07] Stanislav N Gorb, Mitali Sinha, Andrei Peressadko, Kathryn A Daltorio, and Roger D Quinn, *Insects did it first: a micropatterned adhesive tape for robotic applications*, Bioinspiration & biomimetics **2** (2007), no. 4, S117.

[HA05] WR Hansen and K Autumn, *Evidence for self-cleaning in gecko setae*, Proceedings of the National Academy of Sciences of the United States of America **102** (2005), no. 2, 385–389.

[HCM12] Nur Hazlin Hazrin-Chong and Mike Manefield, *An alternative sem drying method using hexamethyldisilazane (hmds) for microbial cell attachment studies on sub-bituminous coal*, Journal of microbiological methods **90** (2012), no. 2, 96–99.

[HG61] Robert Hooke and R. T. Gunther, *Micrographia, or, some physiological descriptions of minute bodies made by magnifying glasses : with observations and inquiries thereupon*, Dover Publications, New York, 1961.

[HG12] Naoe Hosoda and Stanislav N Gorb, *Underwater locomotion in a terrestrial beetle: combination of surface de-wetting and capillary forces*, Proceedings of the Royal Society B: Biological Sciences **279** (2012), no. 1745, 4236–4242.

[HVL+12] Gregor Hlawacek, Vasilisa Veligura, Stefan Lorbek, Tijs F Mocking, Antony George, Raoul van Gastel, Harold JW Zandvliet, and Bene

Poelsema, *Imaging ultra thin layers with helium ion microscopy: Utilizing the channeling contrast mechanism*, Beilstein journal of nanotechnology **3** (2012), no. 1, 507–512.

[IHW+12] Elena P Ivanova, Jafar Hasan, Hayden K Webb, Vi Khanh Truong, Gregory S Watson, Jolanta A Watson, Vladimir A Baulin, Sergey Pogodin, James Y Wang, Mark J Tobin, et al., *Natural bactericidal surfaces: mechanical rupture of pseudomonas aeruginosa cells by cicada wings*, Small **8** (2012), no. 16, 2489–2494.

[JG11] David C Joy and Brendan J Griffin, *Is microanalysis possible in the helium ion microscope?*, Microscopy and Microanalysis **17** (2011), no. 04, 643–649.

[KB07] Tae Wan Kim and Bharat Bhushan, *Adhesion analysis of multi-level hierarchical attachment system contacting with a rough surface*, Journal of Adhesion Science and Technology **21** (2007), no. 1, 1–20.

[KDK+03] M Kohane, A Daugela, H Kutomi, L Charlson, A Wyrobek, and J Wyrobek, *Nanoscale in vivo evaluation of the stiffness of drosophila melanogaster integument during development*, Journal of Biomedical Materials Research Part A **66** (2003), no. 3, 633–642.

[KFG13] Alexander E Kovalev, Alexander E Filippov, and Stanislav N Gorb, *Insect wet steps: loss of fluid from insect feet adhering to a substrate*, Journal of The Royal Society Interface **10** (2013), no. 78, 20120639.

[KKE+11] Michail Kryuchkov, Vladimir L Katanaev, Gennadiy A Enin, Anton Sergeev, Alexander A Timchenko, and Igor N Serdyuk, *Analysis of micro-and nano-structures of the corneal surface of drosophila and its mutants by atomic force microscopy and optical diffraction*, PloS one **6** (2011), no. 7, e22237.

[KLK+12] Jae-Jun Kim, Youngseop Lee, Ha Gon Kim, Ki-Ju Choi, Hee-Seok Kweon, Seongchong Park, and Ki-Hun Jeong, *Biologically inspired led lens from cuticular nanostructures of firefly lantern*, Proceedings of the National Academy of Sciences **109** (2012), no. 46, 18674–18678.

[KMS04] Antonia B Kesel, Andrew Martin, and Tobias Seidl, *Getting a grip on spider attachment: an afm approach to microstructure adhesion in arthropods*, Smart materials and structures **13** (2004), no. 3, 512.

[KS11] David Klocke and Helmut Schmitz, *Water as a major modulator of the mechanical properties of insect cuticle*, Acta biomaterialia **7** (2011), no. 7, 2935–2942.

[Kum12] Justin P Kumar, *Building an ommatidium one cell at a time*, Developmental Dynamics **241** (2012), no. 1, 136–149.

[LD10] Brandon J Loveall and David L Deitcher, *The essential role of bursicon during drosophila development*, BMC developmental biology **10** (2010), no. 1, 92.

[LJP+10] Dennis R LaJeunesse, Brooke Johnson, Jason S Presnell, Kathleen K Catignas, and Grzegorz Zapotoczny, *Peristalsis in the junction region of the drosophila larval midgut is modulated by dh31 expressing enteroendocrine cells*, BMC physiology **10** (2010), no. 1, 14.

[LWSW12] Wen-Di Li, Wei Wu, and Richard Stanley Williams, *Combined helium ion beam and nanoimprint lithography attains 4 nm half-pitch dense patterns*, Journal of Vacuum Science & Technology B **30** (2012), no. 6, –.

[MPG+13] M. Melli, A. Polyakov, D. Gargas, C. Huynh, L. Scipioni, W. Bao, D. F. Ogletree, P. J. Schuck, S. Cabrini, and A. Weber-Bargioni, *Reaching the theoretical resonance quality factor limit in coaxial plasmonic nanoresonators fabricated by helium ion lithography*, Nano Letters **13** (2013), no. 6, 2687–2691.

[MRM+05] Livio Muscariello, Francesco Rosso, Gerardo Marino, Antonio Giordano, Manlio Barbarisi, Gennaro Cafiero, and Alfonso Barbarisi, *A critical overview of esem applications in the biological field*, Journal of cellular physiology **205** (2005), no. 3, 328–334.

[MRS93] V.B. Meyer-Rochow and I.A.N. Stringer, *A system of regular ridges instead of nipples on a compound eye that has to operate near the diffraction limit*, Vision Research **33** (1993), no. 18, 2645 – 2647.

[MSR07] Carsten H.G. Muller, Andy Sombke, and Jorg Rosenberg, *The fine structure of the eyes of some bristly millipedes (penicillata, diplopoda): Additional support for the homology of mandibulate ommatidia*, Arthropod Structure & Development **36** (2007), no. 4, 463 – 476, Origin and Evolution of Arthropod Visual Systems (Part II).

[MYH12] Michael M. Marshall, Jijin Yang, and Adam R. Hall, *Direct and transmission milling of suspended silicon nitride membranes with a focused helium ion beam*, Scanning **34** (2012), no. 2, 101–106.

[Ove67] Jane Overton, *The fine structure of developing bristles in wild type and mutant drosophila melanogaster*, Journal of morphology **122** (1967), no. 4, 367–379.

[PCC+12] Kyoo-Chul Park, Hyungryul J. Choi, Chih-Hao Chang, Robert E. Cohen, Gareth H. McKinley, and George Barbastathis, *Nanotextured silica surfaces with robust superhydrophobicity and omnidirectional broadband supertransmissivity*, ACS Nano **6** (2012), no. 5, 3789–3799.

[PG10] Henrik Peisker and Stanislav N. Gorb, *Always on the bright side of life: anti-adhesive properties of insect ommatidia grating*, The Journal of Experimental Biology **213** (2010), no. 20, 3457–3462.

[Pre11] Etheresia Pretorius, *Traditional coating techniques in scanning electron microscopy compared to uncoated charge compensator technology: Looking at human blood fibrin networks with the zeiss ultra plus fegsem*, Microscopy research and technique **74** (2011), no. 4, 343–346.

[RHS+06] Nan Ren, Biao He, David Stone, Sreenatha Kirakodu, and Paul N Adler, *The shavenoid gene of drosophila encodes a novel actin cytoskeleton interacting protein that promotes wing hair morphogenesis*, Genetics **172** (2006), no. 3, 1643–1653.

[RS97] V. Raineri and M. Saggio, *Radiation damage and implanted he atom interaction during void formation in silicon*, Applied Physics Letters **71** (1997), no. 12, 1673–1675.

[RvVM+13] Maria Rudneva, Emile van Veldhoven, Sairam K. Malladi, Diederik Maas, and Henny W. Zandbergen, *Novel nanosample preparation with a helium ion microscope*, Journal of Materials Research **28** (2013), 1013–1020.

[RW00] Jozef Razowski and Janusz Wojtusiak, *Cornea of ommatidia in lepidoptera (insecta) – a scanning electron microscope study*, Folia Biologica **54** (2006-06-01T00:00:00), no. 1-1, 49–53.

[SACF+12] Johannes Schindelin, Ignacio Arganda-Carreras, Erwin Frise, Verena Kaynig, Mark Longair, Tobias Pietzsch, Stephan Preibisch, Curtis Rueden, Stephan Saalfeld, Benjamin Schmid, Jean-Yves Tinevez,

Daniel James White, Volker Hartenstein, Kevin Eliceiri, Pavel Tomancak, and Albert Cardona, *Fiji: an open-source platform for biological-image analysis*, Nat Meth **9** (2012), no. 7, 676–682.

[Sch11] Heide Schatten, *Low voltage high-resolution sem (lvhrsem) for biological structural and molecular analysis*, Micron **42** (2011), no. 2, 175–185.

[SFPA06] Doekele G Stavenga, S Foletti, G Palasantzas, and Kentaro Arikawa, *Light on the moth-eye corneal nipple array of butterflies*, Proceedings of the Royal Society B: Biological Sciences **273** (2006), no. 1587, 661–667.

[SS93] Elizabeth M. Slayter and Henry S. Slayter, *Light and electron microscopy*, Cambridge University Press, New York, 1993.

[STD74] Bertha FA Stumm-Tegethoff and AW Dicke, *Surface structure of the compound eye of various drosophila species and eye mutants of drosophila melanogaster*, TAG Theoretical and Applied Genetics **44** (1974), no. 6, 262–265.

[SVELS12] Prabuddha Sengupta, Schuyler Van Engelenburg, and Jennifer Lippincott-Schwartz, *Visualizing cell structure and function with point-localization superresolution imaging*, Developmental Cell **23** (2012), 1092–1102.

[TCE12] Nicholas J Tardi, Martha E Cook, and Kevin A Edwards, *Rapid phenotypic analysis of uncoated drosophila samples with low-vacuum scanning electron microscopy*, Fly **6** (2012), no. 3, 184–192.

[TCR+03] Lewis G Tilney, Patricia S Connelly, Linda Ruggiero, Kelly A Vranich, and Gregory M Guild, *Actin filament turnover regulated by cross-linking accounts for the size, shape, location, and number of actin bundles in drosophila bristles*, Molecular biology of the cell **14** (2003), no. 10, 3953–3966.

[TCSG96] Lewis G Tilney, Patricia Connelly, Stacey Smith, and Gregory M Guild, *F-actin bundles in drosophila bristles are assembled from modules composed of short filaments.*, The Journal of cell biology **135** (1996), no. 5, 1291–1308.

[TGCZ94] Barbara J Thomas, Dorian A Gunning, Jennifer Cho, and S Lawrence Zipursky, *Cell cycle progression in the developing drosophila eye:*

roughex encodes a novel protein required for the establishment of g1, Cell **77** (1994), no. 7, 1003–1014.

[TSC+08] Ana Talamillo, Jonatan Sánchez, Rafael Cantera, Coralia Pérez, David Martín, Eva Caminero, and Rosa Barrio, *Smt3 is required for drosophila melanogaster metamorphosis*, Development **135** (2008), no. 9, 1659–1668.

[TTG95] Lewis G Tilney, Mary S Tilney, and Gregory M Guild, *F actin bundles in drosophila bristles. i. two filament cross-links are involved in bundling.*, The Journal of cell biology **130** (1995), no. 3, 629–638.

[VBFSHW12] WS Vanden Berg-Foels, L Scipioni, C Huynh, and X Wen, *Helium ion microscopy for high-resolution visualization of the articular cartilage collagen network*, Journal of microscopy **246** (2012), no. 2, 168–176.

[VGT+12] Timothée Vignaud, Rémi Galland, Qingzong Tseng, Laurent Blanchoin, Julien Colombelli, and Manuel Théry, *Reprogramming cell shape with laser nano-patterning*, Journal of Cell Science **125** (2012), no. 9, 2134–2140.

[WCM+09] D. Winston, B. M. Cord, B. Ming, D. C. Bell, W. F. DiNatale, L. A. Stern, A. E. Vladar, M. T. Postek, M. K. Mondol, J. K. W. Yang, and K. K. Berggren, *Scanning-helium-ion-beam lithography with hydrogen silsesquioxane resist*, Journal of Vacuum Science and Technology B Microelectronics and Nanometer Structures **27** (2009), no. 6, 2702–2706.

[WCW10] Gregory S Watson, Bronwen W Cribb, and Jolanta A Watson, *How micro/nanoarchitecture facilitates anti-wetting: an elegant hierarchical design on the termite wing*, ACS nano **4** (2010), no. 1, 129–136.

[Wig85] VB Wigglesworth, *Sclerotin and lipid in the waterproofing of the insect cuticle*, Tissue and Cell **17** (1985), no. 2, 227–248.

[WMN+11] Donald Winston, Vitor R. Manfrinato, Samuel M. Nicaise, Lin Lee Cheong, Huigao Duan, David Ferranti, Jeff Marshman, Shawn McVey, Lewis Stern, John Notte, and Karl K. Berggren, *Neon ion beam lithography (nibl)*, Nano Letters **11** (2011), no. 10, 4343–4347.

[WUF00] Jonathan D Wasserman, Sinisa Urban, and Matthew Freeman, *A family of rhomboid-like genes: Drosophila rhomboid-1 and roughoid/rhomboid-3 cooperate to activate egf receptor signaling*, Genes & Development **14** (2000), no. 13, 1651–1663.

[YDRGG08] H Yao, G Della Rocca, PR Guduru, and H Gao, *Adhesion and sliding response of a biologically inspired fibrillar surface: experimental observations*, Journal of The Royal Society Interface **5** (2008), no. 24, 723–733.

[YFS+11] Jijin Yang, David C Ferranti, Lewis A Stern, Colin A Sanford, Jason Huang, Zheng Ren, Lu-Chang Qin, and Adam R Hall, *Rapid and precise scanning helium ion microscope milling of solid-state nanopores for biomolecule detection*, Nanotechnology **22** (2011), no. 28, 285310.